ORIGINAL ARTICLE

Cascade two-stage tumor re-oxygenation and immune re-sensitization mediated by self-assembled albumin-sorafenib nanoparticles for enhanced photodynamic immunotherapy

Zaigang Zhou[a,d,†], Jiashe Chen[b,†], Yu Liu[a,†], Chunjuan Zheng[c], Wenjuan Luo[c], Lele Chen[b], Shen Zhou[b], Zhiming Li[b,*], Jianliang Shen[a,d,e,*]

[a]*State Key Laboratory of Ophthalmology, Optometry and Vision Science, School of Ophthalmology and Optometry, School of Biomedical Engineering, Wenzhou Medical University, Wenzhou 325027, China*
[b]*Department of the First Affiliated Hospital of Wenzhou Medical University, Wenzhou 325000, China*
[c]*School & Hospital of Stomatology, Wenzhou Medical University, Wenzhou 325027, China*
[d]*Wenzhou Institute, University of Chinese Academy of Sciences, Wenzhou 325000, China*
[e]*Oujiang Laboratory (Zhejiang Lab for Regenerative Medicine, Vision and Brain Health), Wenzhou 325000, China*

Abstract As a promising modality for cancer therapy, photodynamic therapy (PDT) still acquired limited success in clinical nowadays due to the extremely serious hypoxia and immunosuppression tumor microenvironment. To ameliorate such a situation, we rationally designed and prepared cascade two-stage re-oxygenation and immune re-sensitization BSA-MHI148@SRF nanoparticles *via* hydrophilic and hydrophobic self-assembly strategy by using near-infrared photodynamic dye MHI148 chemically modified bovine serum albumin (BSA-MHI148) and multi-kinase inhibitor Sorafenib (SRF) as a novel tumor oxygen and immune microenvironment regulation drug. Benefiting from the accumulation of SRF in tumors, BSA-MHI148@SRF nanoparticles dramatically enhanced the PDT efficacy by promoting cascade two-stage tumor re-oxygenation mechanisms: (i) SRF decreased tumor oxygen consumption *via* inhibiting mitochondria respiratory. (ii) SRF increased the oxygen supply *via* inducing tumor vessel normalization. Meanwhile, the immunosuppression micro-environment was also obviously reversed by

*Corresponding authors. Tel./fax: +1 315 7372733 (Jianliang Shen); Tel./fax: + 1 598 8718867 (Zhiming Li).

E-mail addresses: zhi-mingli@163.com (Zhiming Li), shenjl@wiucas.ac.cn (Jianliang Shen).

†These authors made equal contributions to this work.

two-stage immune re-sensitization as follows: (i) Enhanced immunogenic cell death (ICD) production amplified by BSA-MHI148@SRF induced reactive oxygen species (ROS) generation enhanced T cell infiltration and improve its tumor cell killing ability. (ii) BSA-MHI148@SRF amplified tumor vessel normalization by VEGF inhibition also obviously reversed the tumor immune-suppression microenvironment. Finally, the growth of solid tumors was significantly depressed by such well-designed BSA-MHI148@SRF nanoparticles, which could be potential for clinical cancer therapy.

1. Introduction

As a therapeutic method for various diseases, photodynamic therapy (PDT) with the advantages of noninvasiveness, high spatiotemporal controllability, and favorable safety has been regarded as a promising modality of cancer therapy over the past decades[1,2]. In the process of PDT, the reactive oxygen species (ROS) is generated *via* photosensitizer with laser irradiation in the presence of molecular oxygen to kill cancer cells[3–5]. Besides, PDT could also reverse "cold" tumors to "hot" tumors for immunotherapy by inducing T lymphocyte infiltration and enhancing its activity[6]. However, since the ROS generation of PDT relies on oxygen supply which was sparse in solid tumors, the efficiency of PDT toward tumors is still severely restricted[7]. Besides, after PDT treatment, PD-L1 expression in the tumors is significantly increased by the enhanced interferon γ (IFN-γ) generation in some cases, inducing the immune tolerance[8,9]. Therefore, how to effectively reverse the tumor hypoxia and immunosuppressive microenvironment to enhance the PDT efficacy has been on the agenda to solve these days.

Facing these challenges, tremendous efforts are being made to ameliorate the hypoxia environment through tumor-targeted oxygen delivery or endogenous oxygen generation strategy with the benefit of cell intracellular catalysis[10–12]. Unfortunately, these methods could only relieve tumor hypoxia temporarily and still cannot settle the problem of tumor hypoxia fundamentally, leading to poor PDT therapeutic effect[13–15]. As we all know, although the "Warburg effect" was the main source of tumor energy, the excessive tumor cell mitochondria-associated oxidative phosphorylation (OXPHOS) still appears in a lot of tumor cell lines to induce the overwhelming physiological O_2 consumption, leading to more remarkable tumor hypoxia[16,17]. Importantly, computational models also predict that decreasing intrinsic O_2 consumption would more effectively mitigate the hypoxia status[16,18]. According to this theory, numerous potent mitochondria-associated oxidative phosphorylation disrupting drugs like lonidamine, metformin, atovaquone, and tamoxifen have been proposed to reduce oxygen consumption *via* disrupting OXPHOS to solve tumor hypoxia[19–22]. This opens a new route toward the reversal of tumor hypoxia-triggered PDT tolerance, but the efficacy of these drugs is still restricted since none of these drugs could be effectively used in clinical for different defects, like too high a dose needed for Metformin and widespread drug resistance for Tamoxifen[23,24]. Hence, an effective alternative clinical useable drug is still demanded for tumor re-oxygenation to enhance the PDT efficacy.

Apart from this, it is generally known that the O_2 content in tumor cells depends on the oxygen supply from blood and the oxygen consumption by tumor cells[25,26]. Owing to the inadequate oxygen supply induced by immature and abnormal tumor blood vessels, it seems that only boosting the tumor re-oxygenation by cutting oxygen consumption is still not that sufficient[25,27]. Multistage oxygen regulation strategy that could enhance oxygen perfusion and decrease oxygen consumption simultaneously is still necessary to better reverse tumor hypoxia[25,27]. Given this theory, it is noticed that tumor vessel normalization mediated by vascular endothelial growth factor (VEGF) inhibition could reverse the tumor hypoxia microenvironment by increasing oxygen supply[28–30]. Interestingly enough, Sorafenib (SRF), a typical VEGF inhibitor with effective tumor vessel normalization capacity is newly proved to possess the capacity to reduce tumor oxygen consumption rate by inhibiting OXPHOS[31,32]. Thus, SRF may be feasible to be used as a cascade two-stage tumor re-oxygenation strategy with the vascular normalization to enhance oxygen perfusion and mitochondrial respiratory inhibition to decrease oxygen consumption capacity to better promote PDT efficacy.

After some PDT treatments, the expression of programmed cell death ligand 1 (PD-L1) in the tumor is significantly increased by increased IFN-γ production, which then leads to the immune tolerance of tumors to immune cells[8,9,33]. Fortunately, mitochondrial OXPHOS depression mediated AMP-activated protein kinase (AMPK) phosphorylation has been newly demonstrated to inhibit the expression of PD-L1 protein *via* endoplasmic reticulum-associated protein degradation[8,34]. Besides, it is confirmed that using mitochondria-associated oxidative phosphorylation disrupting drugs to break PD-L1 and PD-1 interaction rather than the expensive and toxic PD-L1 antibody could better and more suitably augment the efficacy of chemotherapy, PDT, or photothermal therapy[8,23,34,35]. Sorafenib (SRF), a typical VEGF inhibitor with effective tumor vessel normalization capacity is newly proved to possess the ability to induce AMPK activation, meaning that SRF may also decrease PD-L1 expression to reverse tumor immunosuppressive microenvironment, which has not been proven yet[36]. Moreover, by inducing tumor vessel normalization, not only tumor hypoxia microenvironment could be reversed but also the immunosuppressive microenvironment is relieved with enhanced T cell infiltration and antitumor immune activity[37,38]. Thus, SRF may be used as a cascade two-stage immune re-sensitization drug through downregulating PD-L1 expression and inducing tumor vessel normalization to enhance T cell infiltration.

Based on the above background, in this study, we rationally designed and prepared the cascade two-stage tumor re-oxygenation and immune re-sensitization regulation BSA-MHI148@SRF nanoparticles by hydrophilic and hydrophobic self-assembly strategy (Fig. 1). The near-infrared photodynamic dye MHI148 chemically modified bovine serum albumin (BSA-MHI148) was used as
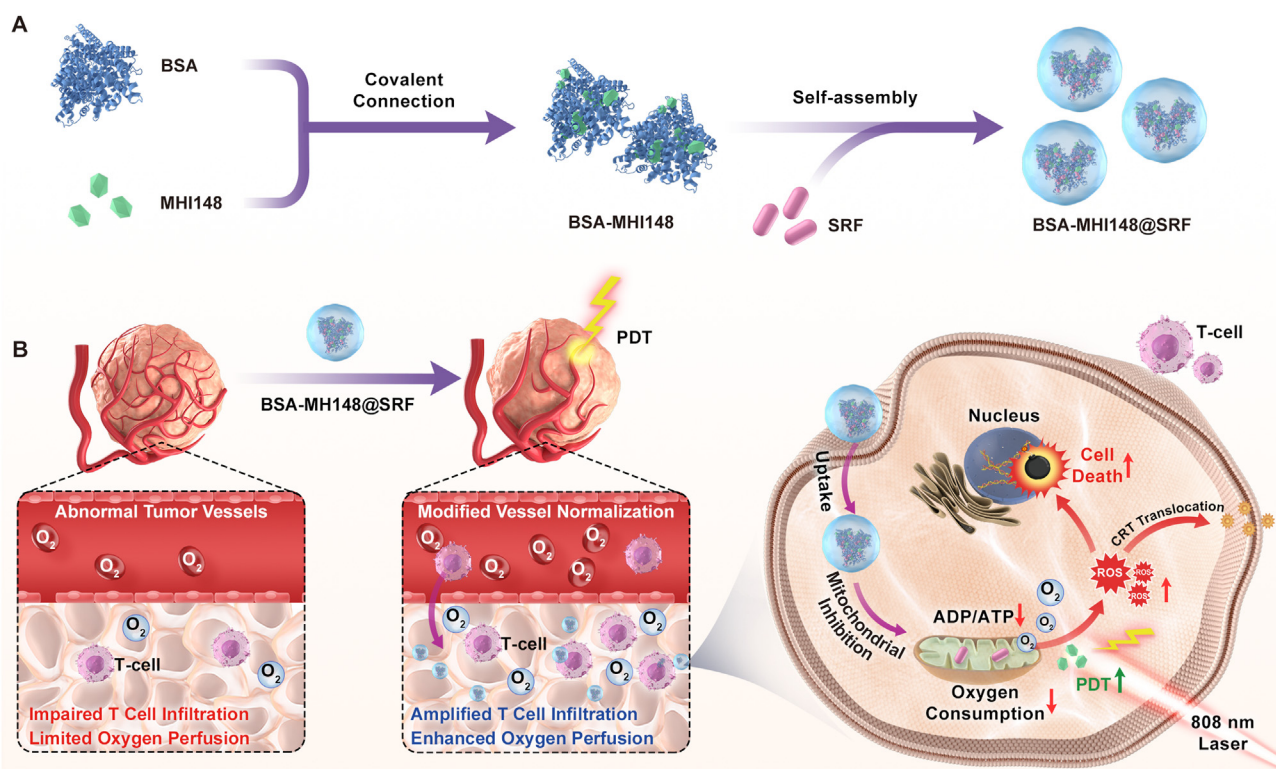
Figure 1 (A) Schematic illustration of the synthesis route of BSA-MHI148@SRF nanoparticles. (B) The mechanism of BSA-MHI148@SRF nanoparticles mediated cascade two-stage re-oxygenation and immune re-sensitization strategy for enhanced tumor photodynamic immunotherapy.

the hydrophobic drug carrier, and the multi-kinase inhibitor SRF as novel tumor oxygen and immune microenvironment regulation drug. Benefiting from the tumor active targeting capacity of BSA-MHI148, BSA-MHI148@SRF nanoparticles could selectively accumulate in the tumor tissues. Then, SRF encapsulated in BSA-MHI148@SRF nanoparticles was expected to normalize the tumor vessels by VEGF inhibition to enhance oxygen perfusion and restrain mitochondrial respiratory to decrease oxygen consumption to maximize tumor re-oxygenation for effective PDT. By doing this, the intracellular MHI148, which was located in mitochondria, could generate amounts of ROS to cause the ICD of tumor cells for further anti-tumor immune response under laser irradiation. Moreover, the amplified VEGF inhibition induced by BSA-MHI148@SRF nano-particles could also obviously reverse the tumor immune-supp-ression microenvironment by causing tumor vessel normalization. In consequence, the growth of solid tumors was significantly depr-essed by this well-designed BSA-MHI148@SRF nanoparticles. Given these encouraging results, the strategy might provide a safe and effective approach for better cancer PDT treatment in the near future.

2. Materials and methods

2.1. Materials

Sorafenib (SRF), bovine serum albumin (BSA), and dimethyl sulfoxide (DMSO) were purchased from Aladdin Co., Ltd. (Shanghai, China). MHI148 was provided from Heowns Business License (Tianjin, China). *N,N*-Dimethylformamide (DMF) and

4-(4,6-dimethoxy-1,3,5-triazin-2-yl)-4-methylmorpholinium chlo-ride (DMTMM) were obtained from Aladdin Co., Ltd. (Shanghai, China). DCFH-DA and JC-1 assay kits were purchased from Beyotime Biotechnology (Shanghai, China). ROS-ID hypoxia/oxidative stress detection kit was obtained from Enzo Life Sciences (Farmingdale, NY, USA). Lyso-Tracker Green and Mito-Tracker Green were purchased by Yeasen Biotech Co., Ltd. (Shanghai, China).

2.2. Synthesis of BSA-MHI148

40 mg of MHI148 was dissolved in 4 mL of DMSO. Following this, the solution was mixed with 20 mg of 4-(4,6-dimethoxy [1.3.5]triazin-2-yl)-4-methylmorpholinium chloride hydrate (DM-TMM) in the dark for 1 h. Then, the activated MHI148 was mixed with 2 g BSA dissolved in 200 mL double distilled water. The obtained mixture was stirred for 6 h at room temperature. After that, the pure BSA-MHI148 was acquired after the dialysis (MW = 10 kDa) with pure H_2O 5 times to remove free MHI148, DMTMM, and DMSO. Finally, the final BSA-MHI148 powder was obtained by vacuum freeze-drying.

2.3. Preparation and characterization of BSA-MHI148@SRF nanoparticles

The BSA-MHI148@SRF nanoparticles were prepared by one-step hydrophilic and hydrophobic self-assembly strategy. Generally, 3 mg SRF was dissolved in 250 μL DMF, which then was drop-wise added into the 50 mL BSA-MHI148 solution (2 mg/mL).

After stirring for 30 s, the solution was purified by ultrafiltration (MW = 30 kDa) to remove the un-encapsulated SRF by an Amicon® Ultrafiltration cup.

The morphology of BSA-MHI148@SRF nanoparticles was characterized by transmission electron microscopy (TEM, FEI Talos F200S, Thermo Fisher Scientific, Cleveland, OH, USA). The distribution of the particle size and zeta potential was analyzed with a Zetasizer (Zetasizer Nano ZS ZEN3600, Malvern, UK). The loading efficiency (LE) and encapsulation efficiency (EE) of SRF were determined by high-performance liquid chromatography (HPLC, Agilent 1260, Santa Clara, CA, USA) and UV−Vis spectrometer (Lambda 25, PerkinElmer, Waltham, MA, USA), respectively.

LE and EE were calculated as the following Eqs. (1) and (2):

$$\text{LE (\%)} = (\text{Weight of SRF in BSA-MHI148@SRF / Total weight of BSA-MHI148@SRF}) \times 100 \tag{1}$$

$$\text{EE (\%)} = (\text{Weight of SRF loaded in BSA-MHI148@SRF / Total weight of SRF fed initially}) \times 100 \tag{2}$$

2.4. Cell culture and animals

Murine bladder tumor MB49 cells, murine melanoma B16F10 cells, murine breast tumor 4T1 cells, and human non-small cell lung tumor A549 cells were provided from the American Type Culture Collection. 4T1 cells and A549 cells were cultured in Dulbecco's modified Eagle's medium (DMEM, Gibco, Grand Island, NY, USA), while others in Roswell Park Memorial Institute (RPMI-1640, Gibco, Grand Island, NY, USA), containing 10% fetal bovine serum (FBS, Gibco, Grand Island, NY, USA) and 1% streptomycin/penicillin at 37 °C with 5% CO_2 in a biosafety cabinet (Thermal Fisher Inc, Waltham, MA, USA).

Female C57BL/6 mice (7−8 weeks old, 19−21 g) mice were supplied from the Experiment Animal Center of Wenzhou Medical University (China). All animal tests were performed in accordance with the Experimental Animal Administration Committee of Zhejiang Province and the ethical guidelines for animal experiments of Wenzhou Medical University.

2.5. Western blotting

Western blotting analysis was performed according to our previous study[8,35]. Briefly, cell samples or mouse tumor tissues were lysed by RIPA lysis buffer containing protease, phenylmethanesulfonyl fluoride, and phosphatase inhibitors. Bicinchoninic acid (BCA) protein assay was carried out to determine the total protein concentrations. Next, proteins were separated by 10% SDS-polyacrylamide gel electrophoresis and the protein bands were further electro-transferred onto the PVDF membrane. Subsequently, the PVDF membranes were incubated at 4 °C with corresponding primary antibodies against Vinculin (1:1000, Affinity, Temecula, CA, USA), phosphoSTAT1 (1:1000, Affinity), total STAT1 (1:1000, Affinity), PD-L1 (1:1000, Affinity), β-actin (1:5000, Affinity), AMPK (1:1000, CST, Danvers, MA, USA), phospho-AMPK (Thr 172, 1:1000, CST), HIF-1α (1:1000, Affinity), CD31 (1:1000, Affinity), α-SMA (1:1000, Affinity), and VEGF (1:1000, Affinity) with gentle shaking overnight. 24 h later, the membranes were exposed to secondary antibodies at room temperature for another 2 h. Finally, the images of the protein bands were acquired by using the Fluorescent & Chemiluminescence Gel Imaging System (Peiqing Science and Technology Co., Ltd., Shanghai, China).

2.6. Detection of singlet oxygen in vitro

The singlet oxygen generation capacity of BSA-MHI148@SRF nanoparticles was detected by using 3-diphenylisobenzofuran (DPBF). BSA-MHI148@SRF containing MHI148 (2 μmol/L) was mixed with DPBF (25 μmol/L) in double-distilled water. After laser irradiation (808 nm, 100 mW/cm^2, 10 min), the absorption value at 426 nm and corresponding absorption spectra were recorded at the predetermined time.

For intracellular ROS detection, the probe 2′,7′-dichlorodihydrofluorescein diacetate (DCFH-DA) was utilized to assess the ROS generation ability of BSA-MHI148@SRF in the case of hypoxia (1% O_2). Generally, MB49 cells were grown at confocal dishes overnight under normoxic conditions (20% O_2). After that, the cells were treated with SRF, free MHI148, BSA-MHI148, and BSA-MHI148@SRF (2 μmol/L MHI148, 6.58 μmol/L SRF) for 6 h in the case of hypoxia (1% O_2). Subsequently, the cells were washed with PBS twice and incubated with fresh serum-free medium containing 10 μmol/L DCFH-DA for 30 min in the dark, and then irradiated with an 808 nm xenon lamp (100 mW/cm^2, 10 min). Finally, the fluorescence intensity was determined and fluorescence images were acquired using a confocal laser scanning microscope (CLSM, Nikon, Japan).

2.7. Cellular uptake mechanism of BSA-MHI148@SRF nanoparticles

MB49 cells were seeded in confocal dishes or 6-wells plates and cultured overnight. Subsequently, the cells were incubated with 2 μmol/L BSA-MHI148@SRF (calculated by MHI148 concentration) for different time. CLSM and flow cytometry assay were then utilized to determine the cellular fluorescence of MHI148.

For the investigation of the cellular uptake mechanism, 1.5×10^4 MB49 cells were cultured at confocal dishes for 24 h. Following this, the cells were pretreated with 2-deoxy-D-glucose (2-DG), sulfobromophthalein (BSP), and 4 °C for 30 min. Then, cells were incubated with 2 μmol/L BSA-MHI148@SRF nanoparticles (calculated by MHI148 concentration) for another 4 h before the observation of the cellular fluorescence by CLSM.

2.8. In vitro subcellular distribution of BSA-MHI148@SRF nanoparticles

MB49 cells were first seeded in confocal dishes and cultured overnight. Then, the medium was replaced by the fresh medium with 2 μmol/L BSA-MHI148@SRF nanoparticles (calculated by MHI148 concentration). Four hours later, the cells were washed with PBS and then stained by Mitotracker or Lysotracker. Subsequently, the cells were washed three times before the CLSM image collection.

2.9. Cell viability assay

Cell viability of MB49 cells and B16F10 cells after various treatments was determined through Cell Counting Kit-8 (CCK-8) assay. Briefly, MB49 cells and B16F10 cells were seeded in 96-well culture plates with RPMI-1640 medium and DMEM medium respectively under the standard condition. Subsequently, the tumor cells were treated with SRF, free MHI148, BSA-MHI148, and BSA-MHI148@SRF at various concentrations for 24 h in the case of hypoxia (1% O_2) or normoxia (20% O_2). After being washed with PBS twice, some group was irradiated with an

808 nm xenon lamp (100 mW/cm^2, 10 min), followed by incubation for another 24 h. Finally, the cells were incubated with CCK-8 reagent for 3 h and the absorbance of CCK-8 was detected at a wavelength of 450 nm by a microplate reader (BIO-TEK, Winooski, VT, USA).

2.10.   Live/dead cell staining

MB49 cells were seeded at confocal dishes with 1.5×10^4 cells per dish overnight under normoxic conditions (21% O$_2$). Then, the cells were treated with different drugs or preparations (SRF, free MHI148, BSA-MHI148, and BSA-MHI148@SRF) at 2 μmol/L MHI148, 6.58 μmol/L SRF concentration for 6 h in the hypoxic condition (1% O$_2$), followed by the irradiation with 808 nm laser (100 mW/cm^2, 10 min). Subsequently, the calcein-AM/PI reagents were added into the dishes for 30 min to stain the live cells and dead cells in the dark. At last, the cells were washed three times and photographed using CLSM.

2.11.   Cell apoptosis analysis

Cell apoptosis of MB49 cells after various treatments was assessed by using flow cytometry. After being incubated in the normoxic conditions overnight, the MB49 cells were treated with various preparations (SRF, free MHI148, BSA-MHI148, BSA-MHI148@SRF) at 2 μmol/L MHI148, 6.58 μmol/L SRF concentration for 6 h in the hypoxic condition (1% O$_2$). Subsequently, the cells were irradiated with an 808 nm xenon lamp (100 mW/cm^2, 10 min) and then incubated in the incubator with the normal condition for 18 h. Next, the cells were collected and stained with Annexin V-FITC/PI reagents for 20 min at room temperature. At last, the cells were washed with cold PBS three times, followed by the flow cytometry analysis.

2.12.   Hypoxia assessment in vivo and in vitro

The *in vitro and in vivo* expression of hypoxia indicator HIF-1α was evaluated by Western blot assay and immunofluorescence staining assay. For the detection of HIF-1α *in vitro*, the MB49 cells were seeded in 6 cm diameter culture dishes or confocal dishes overnight in normal condition. After the treatment of SRF in the case of hypoxia (1% O$_2$) for 24 h, the cells were collected for Western blot analysis or CLSM observation. When the volume of MB49 tumors reached about 150 mm^3, mice were randomly divided and intravenously injected with various preparations (PBS, BSA@SRF, and BSA-MHI148@SRF) once a day. 48 h later, the mice were sacrificed to acquire the tumors for the Western blot analysis and tissue immunofluorescence staining assay.

For intracellular oxygen detection, the MB49 cells were cultured in normal condition overnight. Next, the cells were exposed to various treatments (20% O$_2$, 1% O$_2$, and 1% O$_2$ along with 6.58 μmol/L SRF) for 6 h. Subsequently, washed with PBS twice, the cells were incubated with oxygen probe ROS-ID (Enzo Life Sciences, Farmingdale, NY, USA) for 30 min. Then, the cells were collected and washed with PBS before the flow cytometry analysis. For the observation of CLSM, the cells in the confocal dishes were further incubated with DAPI to label the nuclei. After washing the cells with PBS, the fluorescence images were acquired by using laser confocal microscopy.

The Seahorse XF96 Extracellular Flux Analyzer (Agilent Technologies, Santa Clara, CA, USA) was used to measure the real-time oxygen consumption rate (OCR) of MB49 cells according to the manufacturer's protocol. Briefly, MB49 cells were seeded into 96-well cell plates and incubated at 37 °C, 5% CO$_2$ overnight. Meanwhile, the calibration plate was incubated at 37 °C, in a non-CO$_2$ incubator overnight. Cells were pre-treated with SRF, BSA-MHI148, and BSA-MHI148@SRF at 2 μmol/L MHI148, 6.58 μmol/L SRF concentration for 8 h, followed by replacing the medium with assay medium, and running the protocol until the calibration was completed. The cells were sequentially exposed to the following compounds: oligomycin (inhibitor of ATP synthase; 1 μmol/L), FCCP (uncoupler of OXPHOS; 1 μmol/L), rotenone (inhibitor of complex I; 1 μmol/L), and antimycin A (inhibitor of complex III; 1 μmol/L).

2.13.   Mitochondrial membrane potential detection

Mitochondrial depolarization was detected by using JC-1 mitochondrial membrane potential probe (Beyotime Biotechnology, Shanghai, China). Generally, the MB49 cells were grown in the normal condition overnight. Next, the cells were incubated with various preparations (PBS, SRF, free MHI148, BSA-MHI148, and BSA-MHI148@SRF) at 2 μmol/L MHI148, 6.58 μmol/L SRF concentration for another 12 h after which the cells were labeled with JC-1 reagents for 30 min, Carbonyl cyanide 3-chlorophenylhydrazone (CCCP) was used as the positive control. At last, the fluorescence intensity of cells was observed by using CLSM.

2.14.   Determination of ATP content and ADP/ATP ratio

The MB49 cells were seeded in the 6 cm diameter culture dishes overnight and then incubated with various treatments (PBS, SRF, free MHI148, BSA-MHI148, and BSA-MHI148@SRF) at 2 μmol/L MHI148, 6.58 μmol/L SRF concentration for 24 h. The cells were collected and lysed for the detection of ATP content and ADP/ATP ratio by using the ATP Detection kit got from Beyotime Biotechnology (Shanghai, China) and ADP/ATP Ratio Assay Kit obtained from Vigorous Biotechnology (Beijing, China), respectively.

2.15.   In vitro fluorescence imaging

MB49 cells were injected into the subcutaneous region slightly below the right armpit of C57BL/6 mice for the establishment of tumor model *in vivo*. When the size of MB49 tumors reached 100 mm^3, free MHI148 (1 mg/kg) and BSA-MHI148@SRF (1 mg/kg, calculated by MHI148 concentration) were separately administered by the tail vein injection ($n = 3$). The images of fluorescence distribution in mice were acquired by the multi-mode optical live imaging system (IVIS Lumina XRMS Series III, PerkinElmer, Waltham, MA, USA) at 1, 4, 8, 12, 24, and 48 h. Subsequently, the mice were sacrificed to collect the major tissues and tumors to further observe the bio-distribution of the BSA-MHI148@SRF nanoparticles *via* the live imaging system.

2.16.   In vitro analysis of immune cells

The effects of BSA-MHI148@SRF nanoparticles mediated PDT on the infiltration of T cells in tumors were assessed using MB49 tumor-bearing mice. Generally, C57BL/6 female mice were injected subcutaneously with 2×10^6 MB49 cells below the right armpit. When the volume of MB49 tumors reached around 100 mm^3, the mice were divided into eight groups randomly. Meanwhile, the mice were injected with Saline, BSA, BSA-MHI148, BSA@SRF nanoparticles, and BSA-MHI148@SRF nanoparticles (5 mg/kg SRF,

2.5 mg/kg MHI148) *via* tail vein, respectively. 24 h later, the tumor sites of some mice were irradiated by an 808 nm laser (0.5 W/cm^2, 2 min). After another 24 h, the tumors were collected to evaluate the immune cell infiltration in tumors.

The evaluation process of tumor immune cell infiltration was as below. Generally, part of the tumors was enzymatic degraded. Then, ACK Lysis Buffer was used to remove the red blood cells in tumors. Finally, the cells obtained from tumors were used to detect the CD3$^+$, CD4$^+$ and CD8$^+$ T cells by flow cytometry assay by using FITC labeled CD4 antibodies (Biolegend, San Diego, CA, USA), FITC labeled CD8 antibodies (Biolegend, San Diego, CA, USA), and APC labeled CD3 antibodies (Biolegend, San Diego, CA, USA). Following these, the other part of the tumors was embedded in OCT and cut into 8 μm slices, followed by staining with FITC labeled CD8 antibodies (Biolegend, San Diego, CA, USA) and FITC-labeled CD4 antibodies (Biolegend, San Diego, CA, USA) according to the manufacturer's protocols.

2.17. Tumor therapy efficacy of BSA-MHI148@SRF nanoparticles mediated PDT

The antitumor efficacy of BSA-MHI148@SRF nanoparticles was assessed using MB49 tumor-bearing mice. Generally, C57BL/6 female mice were injected subcutaneously with 2×10^6 MB49 cells below the right armpit. When the volume of MB49 tumors reached around 70 mm^3, the mice were divided into eight groups randomly ($n = 5$). Meanwhile, the mice were injected with Saline, BSA, BSA-MHI148, BSA@SRF nanoparticles, and BSA-MHI148@SRF nanoparticles (5 mg/kg SRF, 2.5 mg/kg MHI148) *via* tail vein, respectively. 24 h later, the tumor sites of some mice were irradiated by an 808 nm laser (0.5 W/cm^2, 2 min). Tumor volume and body weight of mice were evaluated every two days, and the tumor volume of mice was calculated as below: Volume (mm^3) $= 0.5 \times$ width$^2 \times$ length. At last, the mice were euthanized and the tumors were resected to weigh tumors.

2.18. Biosafety evaluation

The female mice were treated with various preparations as described above. Two weeks later, the mice were sacrificed and the major organs were collected for hematoxylin and eosin (H&E) staining. Besides, the blood from the mice was harvested to evaluate the toxic side effects of BSA-MHI148@SRF nanoparticles *via* the detection of alanine aminotransferase (ALT), aspartate aminotransferase (AST), blood urea nitrogen (BUN), and creatinine (CR) by assay kits purchased from the Jiancheng Bioengineering Institute (Nanjing, China).

2.19. Hemolysis assay

The fresh blood obtained from C57BL/6 mice was mixed with anticoagulant sodium citrate for stabilization. Then, the blood was centrifuged at 2000 rpm (Thermal Fisher Inc., Waltham, MA, USA) for 4 min to acquire the red blood cells. Subsequently, various concentrations of BSA-MHI148@SRF nanoparticles were added into the RBCs suspension to determine the hemolysis activity. Meanwhile, the addition of physiological saline was used as a negative control, while distilled water was a positive control. After standing for 2 h at 37 °C, all samples were centrifuged to obtain the supernatants. At last, the ultraviolet absorption of the supernatants at 541 nm was recorded and the corresponding hemolysis ratios were calculated.

2.20. Statistical analysis

All results are presented as means $\pm$ standard deviation (SD). Statistical analysis was performed *via* a two-tailed Student's *t*-test for the comparison of two groups or one-way ANOVA test for the comparison of multiple groups. $^*P < 0.05$ was considered statistically significant; $^{**}P < 0.01$ and $^{***}P < 0.001$ were extremely significant; NS, no significant difference.

3. Results and discussion

3.1. SRF depressed PD-L1 expression in vitro

Recently, it was newly proved that enhanced phosphorylation of AMPK protein effectively induced by metformin could downregulate the tumor surface expression of PD-L1 protein, leading to alleviated tumor immunosuppression microenvironment *via* breaking the PD-1 and PD-L1 recognition[34]. SRF, an anti-tumor drug widely used in the clinic, was also known as a high-efficiency AMPK activator[31]. Thus, SRF may possess the capacity to regulate PD-L1 expression, which was not proved yet before. To prove this conjecture, the impact of SRF on PD-L1 protein expression in different mouse or human tumor cells was evaluated, including MB49, B16F10, A549, and 4T1 cells (Fig. 2). As illustrated in Fig. 2A−F, with the increased AMPK activation, SRF dose-dependently downregulated PD-L1 expression in all these cells (Supporting Information Fig. S1). In line with the data from the Western blot assay, as the results of immunofluorescence assay and flow cytometry assay showed in MB49 cells, SRF blisteringly attenuated the PD-L1 expression on tumor cell membranes (Supporting Information Fig. S2). IFN-γ, notably secreted by T lymphocytes at tumor sites after PDT or chemotherapy, was the most effective PD-L1 expression inducer[8,34]. To forecast the effects of SRF on PD-L1 expression *in vivo*, IFN-γ co-treatment was also evaluated. Excitingly, SRF treatment significantly inhibited the IFN-γ-stimulated PD-L1 expression as well (Fig. 2G and H). All in all, to our best knowledge, for the first time, we confirmed that SRF could inhibit PD-L1 expression in different tumor cells *in vitro*.

To investigate the mechanism of SRF in downregulating PD-L1 expression, the AMPK inhibitor compound C was utilized to block the induced AMPK activation caused by SRF[23]. As expected, compound C partly eliminated the effect of SRF on depressing PD-L1 expression (Fig. 2I−K). Besides, it has been known that the IFN-γ-induced PD-L1 expression is mediated by STAT1 signaling[21,35]. Therefore, we further explored the mechanism of SRF in inhibiting IFN-γ-induced higher PD-L1 expression. As shown in Fig. 2L and M, the Western blot assay presented that SRF reversed the hyperphosphorylation of STAT1 at Tyr701 induced by IFN-γ, indicating that SRF also partly blocked the PD-L1 expression through the interruption of STAT1 signaling. Thus, all these results suggested that SRF decreased PD-L1 expression *via* AMPK and STAT1 signaling regulation in MB49 cells (Fig. 2N).

3.2. Preparation and characterization of the BSA-MHI148@SRF nanoparticles

To better deliver the hydrophobic drug SRF *in vivo*, BSA-MHI148@SRF nanoparticles were prepared by using near-infrared photodynamic dye MHI148 chemically modified bovine serum albumin (BSA-MHI148) as hydrophobic drug carrier *via* one-step hydrophilic and hydrophobic self-assembly strategy. Generally, BSA was chemically connected with MHI148 through
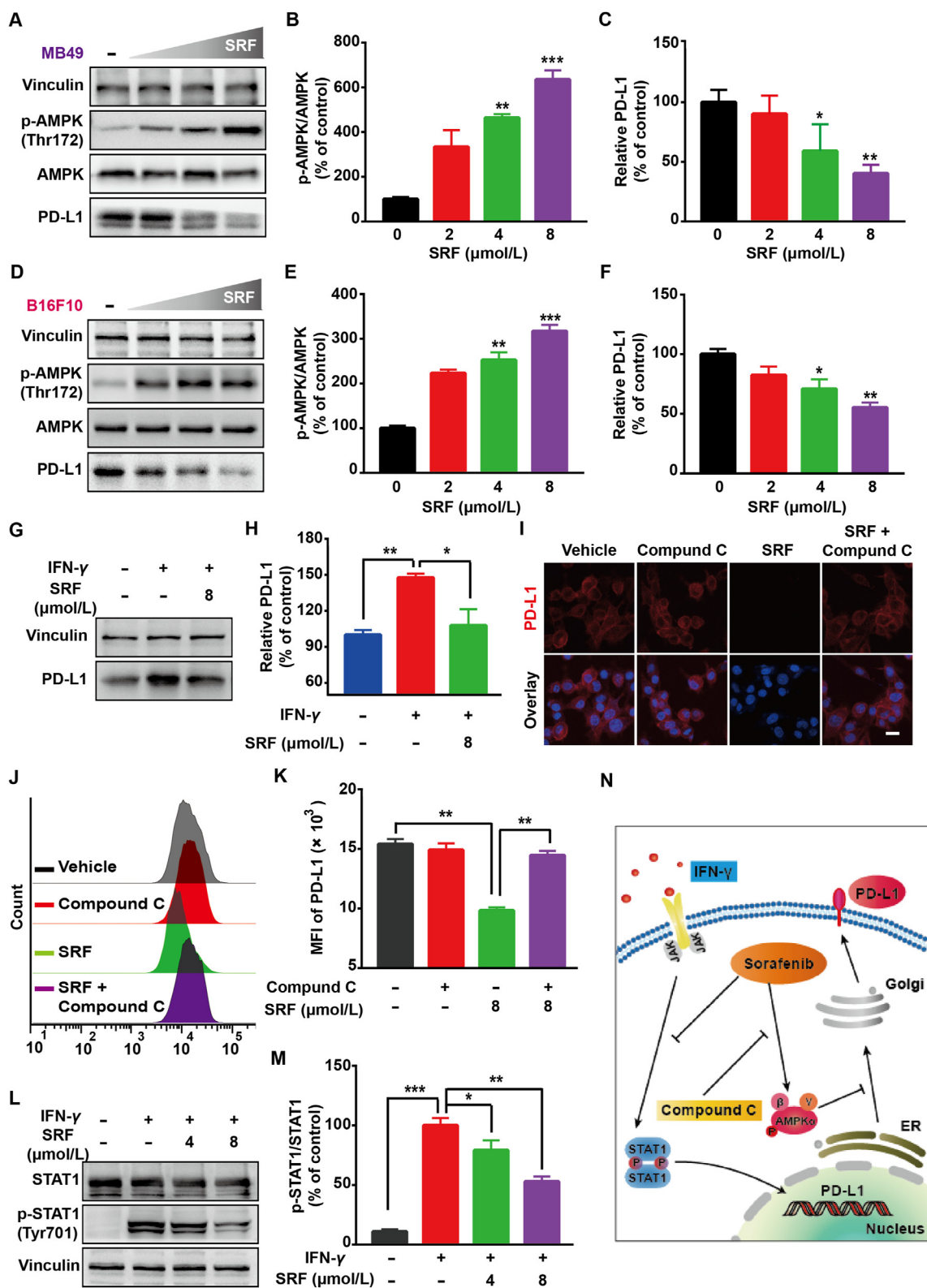
Figure 2 SRF downregulated the expression of PD-L1 in cancer cells through AMPK and STAT1 pathways regulation. (A−F) Expression of the PD-L1 and p-AMPK protein in MB49 and B16F10 tumor cells revealed by Western blot assay and the corresponding protein quantification by ImageJ after the treatment of different concentrations of SRF for 24 h ($n = 3$). (G, H) PD-L1 protein expression in MB49 cells and protein quantification after 20 ng/mL IFN-γ treatment with or without 8 μmol/L SRF for 24 h ($n = 3$). (I−K) The PD-L1 expression in MB49 cells evaluated by immunofluorescent staining and flow cytometry assay after 8 μmol/L SRF treatment in the presence or absence of AMPK inhibitor (20 μmol/L Compound C) ($n = 3$), scale bar = 20 μm. (L, M) Detection of the Tyr701 phosphorylation of STAT1 by Western blot assay after the addition of IFN-γ in the absence or presence of SRF treatment ($n = 3$). (N) Schematic diagram presenting the mechanism of SRF-mediated PD-L1 lower expression. Data are demonstrated as mean ± SD. Statistical analysis was performed *via* the two-tail Student's *t*-test. *$P < 0.05$; **$P < 0.01$; ***$P < 0.001$.
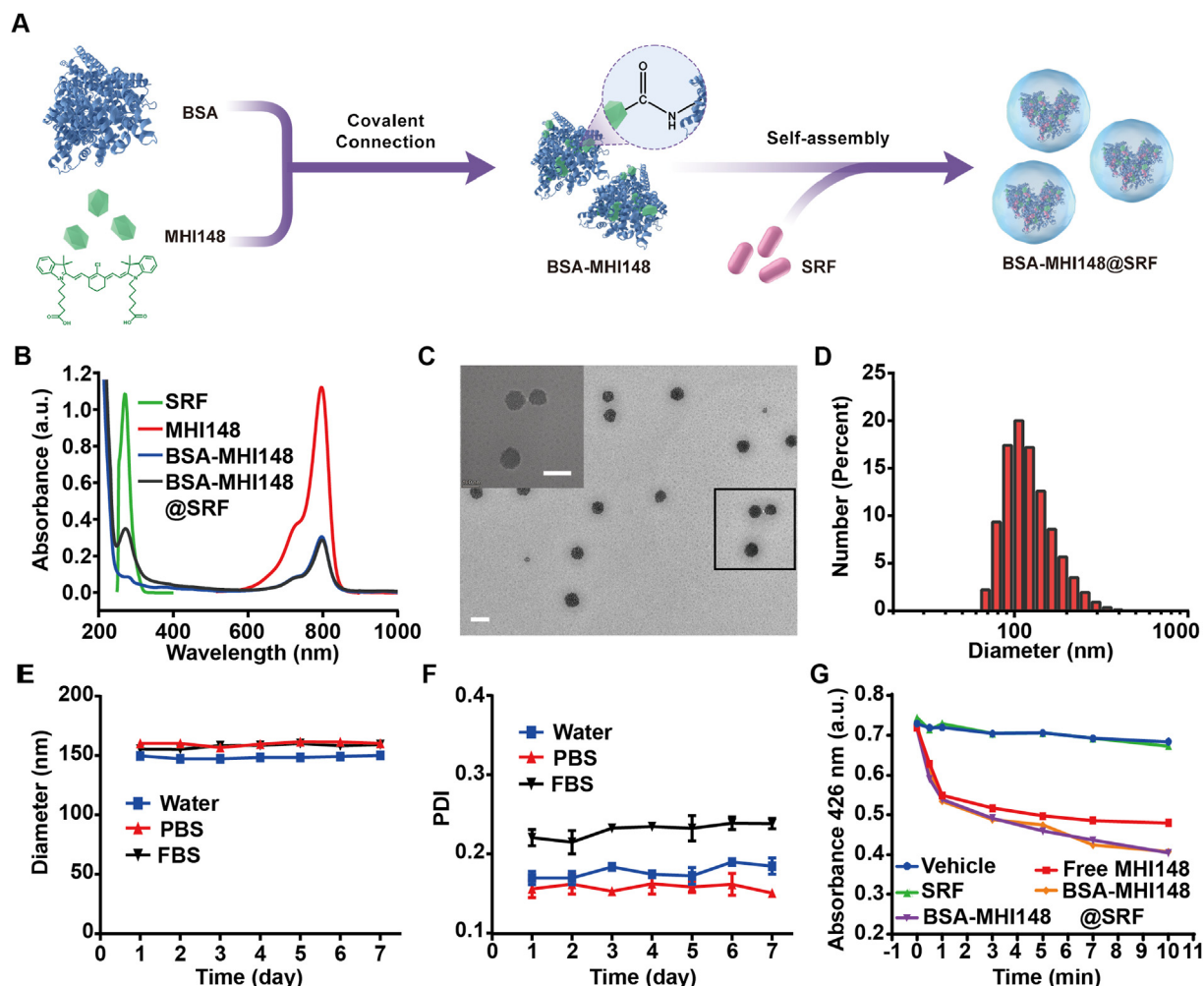
Figure 3 Preparation and characterizations of BSA-MHI148@SRF nanoparticles. (A) Schematic illustration of BSA-MHI148@SRF nanoparticles synthesis process. (B) Absorption spectra of SRF, MHI148, BSA-MHI148, and BSA-MHI148@SRF nanoparticles. (C) TEM images of BSA-MHI148@SRF nanoparticles, scale bars = 200 nm. (D) Hydrodynamic diameters distribution of BSA-MHI148@SRF nanoparticles. (E, F) Hydrodynamic diameter changes and polydispersity index changes of BSA-MHI148@SRF nanoparticles for 7 days in double distilled water, PBS, and FBS ($n = 3$). (G) UV-VIS absorbance of solutions (DPBF, DPBF + SRF, DPBF + free MHI-148, DPBF + BSA-MHI148, and DPBF + BSA-MHI148@SRF nanoparticles) at 426 nm after the 808 nm laser irradiation for different time ($n = 3$). Data are demonstrated as mean $\pm$ SD.

amido bond (Fig. 3A). The UV−Vis absorbance spectrum of BSA-MHI148 showed the typical specific absorption peak of MHI148 at 808 nm, denoting the successful conjugation of MHI148 with BSA (Fig. 3B). Then, BSA-MHI148 could self-assemble with SRF to form BSA-MHI148@SRF nanoparticles *via* hydrophilic and hydrophobic self-assembly interaction (Fig. 3A). The TEM image presented the morphology of BSA-MHI148@SRF with the spherical shape (Fig. 3C). The size distribution and the zeta potential of BSA-MHI148@SRF nanoparticles were 145 ± 10 nm and -13.5 ± 1.1 mV (Fig. 3D, Supporting Information Fig. S3). As examined by HPLC and UV-VIS absorbance spectra, the contents of MHI148 and SRF in BSA-MHI148@SRF nanoparticles were approximately 1.12% and 2.25%, respectively (Supporting Information Fig. S4). Furthermore, to forecast the potential application feasibility of BSA-MHI148@SRF nanoparticles *in vivo*, the stability of BSA-MHI148@SRF nanoparticles was determined by monitoring the

hydrodynamic size and polymer dispersity index (PDI) in double-distilled water, PBS, and the culture medium. No obvious size variations of BSA-MHI148@SRF nanoparticles were detected for 7 days in PBS buffer (pH = 7.4, Fig. 3E and F, Supporting Information Fig. S5), indicating that BSA-MHI148@SRF nanoparticles may possess ideal blood circulation time *in vivo*. As results indicated, like conventional BSA nanoparticles, about 30% SRF encapsulated in BSA-MHI148@SRF would leak out to PBS (pH = 7.4, Supporting Information Fig. S6). In the acid tumor environment simulated by PBS (pH = 6.5) and acid lysosome simulated by PBS (pH = 5.5), more obvious release of SRF from BSA-MHI148@SRF was observed (Fig. S6). Thus, in the acidic tumor microenvironment, SRF could be released from BSA-MHI148@SRF. Then, the singlet oxygen ($^1O_2$) generation capability of BSA-MHI148@SRF was determined by using DPBF, a widely used $^1O_2$ probe. As shown in Fig. 3G, free MHI148, BSA-MHI148, and BSA-MHI148@SRF all displayed a

strong $^1O_2$ generation ability (Supporting Information Fig. S7). All these results above revealed that BSA-MHI148@SRF nanoparticles possessed favorable particle stability, ideal particle size distribution, and outstanding photodynamic efficiency.

3.3. Cell accumulation behavior and mechanism of BSA-MHI148@SRF nanoparticles

The cellular uptake behavior of BSA-MHI148@SRF nanoparticles was then investigated. With the increased incubation time and concentration, the fluorescence intensity of BSA-MHI148@SRF nanoparticles in MB49 cells continuously raised, indicating that tumor cells could effectively uptake BSA-MHI148@SRF nanoparticles (Supporting Information Fig. S8). As is well known, when uptake by normal cells, the antitumor drugs or drug carriers may also induce the obvious cell cytotoxicity to normal cells. Interestingly, previous studies have demonstrated that MHI148 could selectively accumulate in tumor cells rather than normal cells, avoiding pos-sible toxic side effects to normal cells[39,40]. To investigate whether BSA-MHI148 possesses the same tumor cell targeting capacity as free MHI148, tumor cell lines (murine bladder tumor MB49 cells and murine melanoma B16F10 cells), and normal cell lines (murine fibroblasts L929 and human normal hepatocytes LO-2) were utilized. The fluorescence images from the confocal laser scanning microscope (CLSM) also showed that the fluorescence intensity of BSA-MHI148@SRF nanoparticles in the tumor cell lines was much stronger than the normal cell lines (Fig. 4A), which demonstrated the tumor-specific targeting ability of BSA-MHI148@SRF nanoparticles. Thus, BSA-MHI148@SRF nanoparticles could selectively accumulate in the tumor cells rather than in normal cells.

Previous studies have confirmed that the tumor cell targeting capacity of MHI148 was induced by the high-expressed organic anion transporter polypeptide (OATP) in tumor cells[40,41]. Firstly, we evaluated the expression of OTAP-2 and OTAP-8 protein in normal tissue cells and tumor cells (Supporting Information Fig. S9). As results indicated, the OATP-2 and OATP-8 protein expression in MB49 and B16F10 tumor cells was about 4−8-fold of the L929 and LO-2 normal tissue cells (Fig. S9). To further prove whether the cellular uptake mechanism of BSA-MHI148@SRF nanoparticles was also partly mediated by OATP, MB49 cells were pretreated with 2-deoxy-D-glucose (2-DG, an inhibitor of glycolysis), sulfo-bromophthalein (BSP, a competitive inhibitor of OATP transporters) or at 4 °C, respectively, followed by BSA-MHI148@SRF nanoparticles co-incubation. Interestingly, the cellular uptake of BSA-MHI148@SRF nanoparticles was also energy and OATP-dependent (Fig. 4B and C). To sum up, BSA-MHI148@SRF preferred to accumulate at the tumor cell mitochondria rather than in normal cells.

Following this, the localization of BSA-MHI148@SRF nanoparticles in cell organelles was also detected. As results shown, BSA-MHI148@SRF nanoparticles favored to co-localize with Mito-Tracker rather than Lyso-Tracker (Pearson's R-value: 0.65 *vs* 0.13, Fig. 4D; Supporting Information Figs. S10 and S11). However, for BSA-Ce6@SRF, more nanoparticles accumulated in Lyso-Tracker (Pearson's R-value: 0.74), showing that BSA nanoparticles favored localizing in the Lysosome (Supporting Information Fig. S12). Thus, the high expressed OATP protein in tumor cells may help BSA-MHI148@SRF nanoparticles to better avoid the phagocytosis of lysosomes to some extent (Fig. 4D). Then, we evaluated the drug distribution of BSA-MHI148 and SRF in BSA-MHI148@SRF nanoparticles in MB49 cells by using BSA-

MHI148@FITC (FITC as a substitute for SRF, Supporting Information Fig. S13). As results shown, the Colocalization Pearson's R-value of FITC and BSA-MHI148 was only about 0.53 at 4 h after drug administration, meaning that SRF was released from BSA-MHI148@SRF to some extent when accumulated in the tumor cells since the acid tumor microenvironment could trigger the release of SRF from BSA-MHI148@SRF at PBS (pH 6.5Supporting Information Fig. S6), as well as its nonspecific leakage from BSA-MHI148@SRF. To sum up, SRF could be released from BSA-MHI148@SRF in the tumor cells.

3.4. BSA-MHI148@SRF nanoparticles inhibited mitochondrial respiration and enhanced the generation of ROS in vitro

Recently, it was newly proved that SRF could effectively reduce the oxygen consumption rate (OCR) by depressing the mitochondrial function[31]. Thus, SRF or BSA-MHI148@SRF may also possess the ability to reverse tumor hypoxia *via* reducing oxygen consumption, which was rarely proved. As expected, the oxygen status in MB49 cells was detected with Hypoxia/Oxidative Stress Detection kit, showing that the hypoxia condition was bleached by BSA-MHI148@SRF nanoparticles since the red fluorescence of the hypoxia detection molecule was reduced (Fig. 4E and F). This indicated that BSA-MHI148@SRF nanoparticles could relieve the hypoxia status of tumor cells, which then was further confirmed by the OCR detection by using seahorse analysis (Fig. 4E and F, Supporting Information Fig. S14). Furthermore, after the depression of mitochondrial function, BSA-MHI148@SRF nanoparticles decreased mitochondrial membrane potential evaluated by using the mitochondrial membrane potential probe, JC-1 reagent (Fig. 4G). More excitingly, BSA-MHI148@SRF nanoparticles also obviously decreased the ATP production, leading to the further significantly increased ADP/ATP ratio in tumor cells (Fig. 4H and I, Supporting Information Fig. S15). As the tumor hypoxia alleviation was propitious to the ROS generation of PDT based on O_2 consumption, the intracellular ROS generation of BSA-MHI148@SRF nanoparticles with laser irradiation was assessed by using the ROS sensor DCFH-DA. As shown in Fig. 4J and Supporting Information Fig. S16, compared to BSA-MHI148 with laser irradiation, BSA-MHI148@SRF nanoparticles with laser irradiation co-treatment blisteringly increased ROS generation owing to decreased oxygen consumption through the inhibition of mitochondrial respiration by SRF. All in all, BSA-MHI148@SRF nanoparticles could effectively inhibit mitochondrial respiration and enhance ROS generation in vitro.

3.5. Cytotoxicity of BSA-MHI148@SRF nanoparticles in vitro

Subsequently, the effects of BSA-MHI148@SRF nanoparticles on regulating tumor cell apoptosis were assessed by flow cytometry. It was observed that BSA-MHI148@SRF nanoparticles with laser irradiation-induced maximal cell apoptosis compared with all other groups (Fig. 5A). Sure enough, MB49 cells treated by BSA-MHI148@SRF nanoparticles with laser irradiation presented more quantity of red fluorescence of PI and less green fluorescence of Calcein, indicating that BSA-MHI148@SRF nanoparticles caused the most significant cytotoxicity to tumor cells (Fig. 5B). Then, the effects of BSA-MHI148@SRF nanoparticles on the expression of Bcl-2 protein which played a vital role in the proliferation of cells were also explored to further confirm its anti-tumor activity (Fig. 5C and D). As results indicated, the Bcl-2 protein expression significantly decreased in the BSA-MHI148@SRF nanoparticles
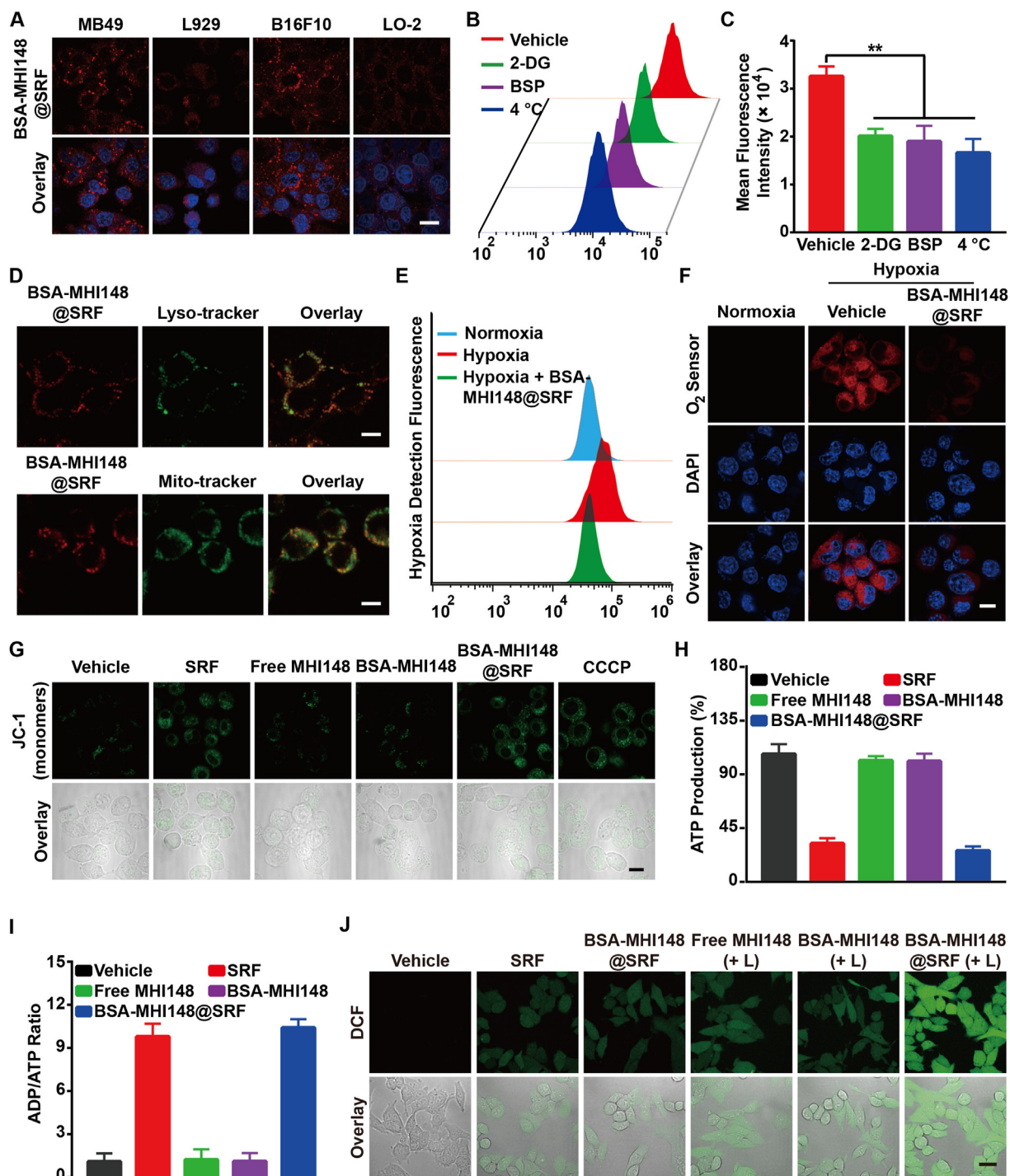
Figure 4 BSA-MHI148@SRF nanoparticles inhibited mitochondrial respiration and enhanced ROS generation *in vitro*. (A) Laser confocal microscope images of BSA-MHI148@SRF nanoparticles uptake in tumor cells (MB49 and B16F10) and normal cells (L929 and LO-2), scale bar = 20 μm. (B, C) Mean fluorescence intensity of BSA-MHI148@SRF nanoparticles in MB49 cells pretreated with 2-deoxy-D-glucose (2-DG), sulfobromophthalein (BSP), and 4 °C (n = 3). (D) Colocalization of BSA-MHI148@SRF nanoparticles with Lysotracker Green-stained lysosomes and Mitotracker Green-stained mitochondria, scale bars = 10 μm. (E) The fluorescence of the O_2 sensor (Hypoxia/Oxidative Stress Detection Kit) in MB49 tumor cells determined by flow cytometry. (F) Representative CLSM images of MB49 cells treated with BSA-MHI148@SRF nanoparticles in the hypoxia condition, the cells were then stained by an O_2 sensor, scale bar = 20 μm. (G) Representative CLSM images of MB49 cells treated with BSA-MHI148@SRF nanoparticles and then stained by JC-1 kit, scale bar = 20 μm. (H, I) Detection of ATP content and ADP/ATP ratio in MB49 cells treated with PBS, SRF, free MHI148, BSA-MHI148, and BSA-MHI148@SRF nanoparticles, respectively (n = 3). (J) Representative CLSM images of the ROS generation detected by DCFH-DA in MB49 cells after different treatments, scale bar = 20 μm. Data are demonstrated as mean ± SD. Statistical analysis was performed *via* the two-tail Student's *t*-test. *$P < 0.05$; **$P < 0.01$; ***$P < 0.001$. (+ L) represented the tumor cells treated with 808 nm laser irradiation.
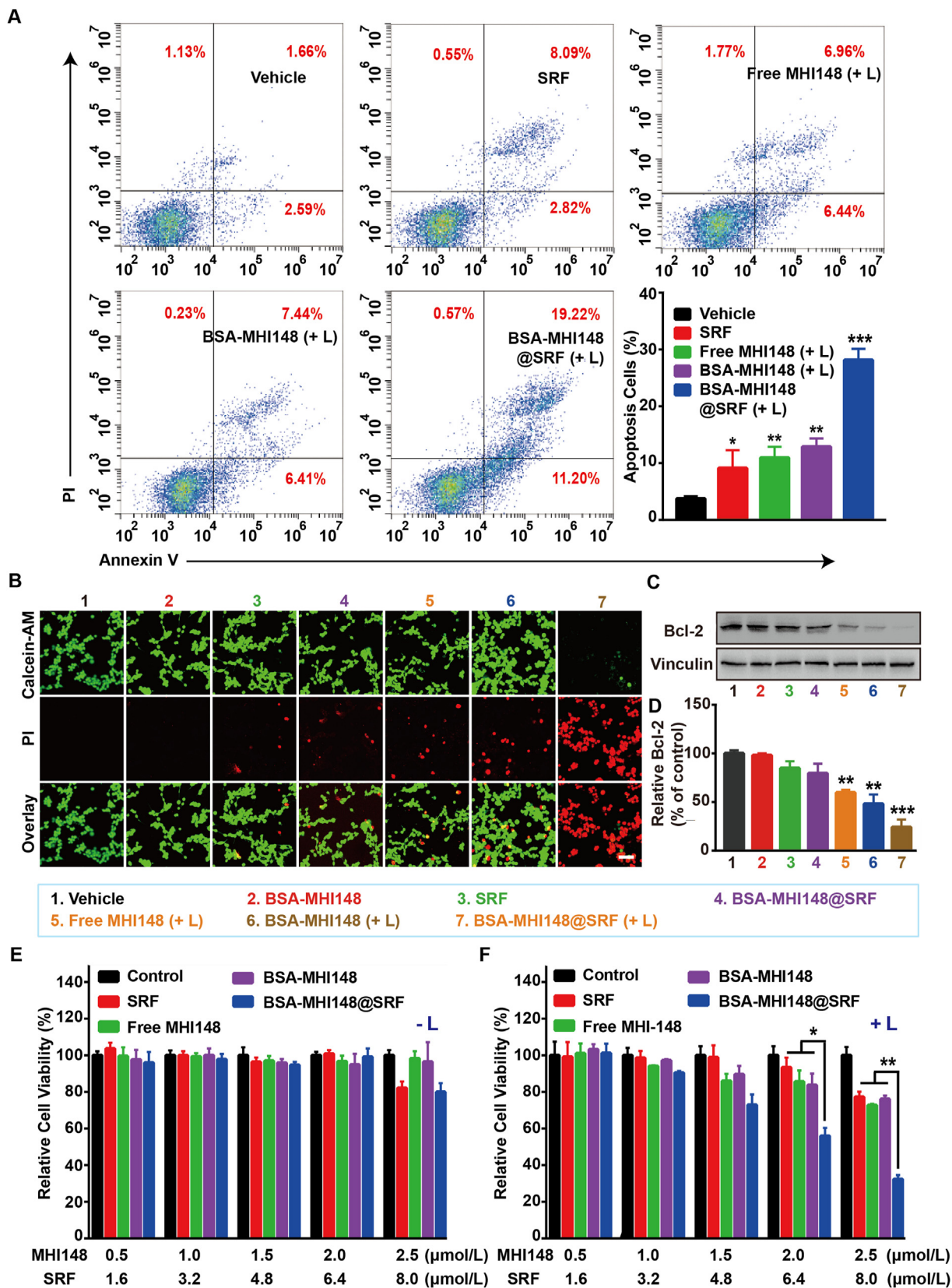
Figure 5 Cytotoxicity of BSA-MHI148@SRF nanoparticles with and without laser radiation *in vitro*. (A) The apoptosis of MB49 cells determined by flow cytometry after treatment with PBS, SRF, free MHI148 + laser irradiation (808 nm, 100 mW/cm^2, 10 min), BSA-MHI148 + laser irradiation, and BSA-MHI148@SRF + laser irradiation. (B) Live/Dead cell staining of MB49 cells after treatment with PBS, BSA-MHI148, SRF, free MHI148 + laser irradiation, BSA-MHI148 + laser irradiation, BSA-MHI148@SRF, and BSA-MHI148@SRF + irradiation, scale bar = 100 μm. (C,

with laser irradiation co-treatment group, followed by BSA-MHI148 with laser irradiation and SRF treatment (Fig. 5C and D). Thus, BSA-MHI148@SRF nanoparticles mediated PDT could most effectively induce tumor cell apoptosis.

Driven by the above positive results, the PDT effects of BSA-MHI148@SRF nanoparticles on MB49 cells or B16F10 cells *in vitro* were then investigated. As shown in Fig. 5E, low-dose BSA-MHI148 treatment without laser irradiation showed negligible cytotoxicity to the MB49 tumor cells. Besides, the cytotoxicity of BSA-MHI148@SRF nanoparticles was also increased in a concentration-dependent manner together with laser irradiation, which was due to the cell-killing effect caused by the SRF encapsulated in it (Fig. 5E). Moreover, BSA-MHI148@SRF nanoparticles with laser irradiation exhibited a more dramatic cell growth inhibition effect than the equal dosage of MHI148 or BSA-MHI148, which was due to the enhanced ROS generation *via* the reversed tumor hypoxia resulting from SRF in it (Fig. 5F). As expected, similar results were also detected in B16F10 cells after the similar treatments (Supporting Information Figs. S17 and S18). Interestingly enough, the concentration of SRF needed to sensitize BSA-MHI148 mediated PDT was only about 8 µmol/L, which was much lower than the antitumor concentration needed for SRF, meaning that SRF may sensitize PDT mainly through hypoxia reversion rather than its antitumor effect (Supporting Information Fig. S19). Collectively, all these results proved that BSA-MHI148@SRF nanoparticles improved the cytotoxicity of PDT *via* the synergistic reaction of SRF and MHI148 mediated PDT.

3.6. BSA-MHI148@SRF nanoparticles inhibited PD-L1 expression and induced immunogenic cell death

Encouraged by the excellent PD-L1 expression inhibition ability of SRF, the effect of BSA-MHI148@SRF nanoparticles on PD-L1 expression in MB49 cells was then assessed. As shown in Fig. 6A–D, BSA-MHI148@SRF nanoparticles displayed obvious down-regulated PD-L1 protein expression and enhanced AMPK activation, which was similar to the free SRF. In addition, results of the flow cytometry assay also demonstrated that IFN-γ-induced higher PD-L1 expression was blocked by BSA-MHI148@SRF nanoparticles (Fig. 6E). From the results above, BSA-MHI148@SRF nanoparticles possessed some admirable features such as PD-L1 expression inhibition capacity like SRF.

Previous research demonstrated that mitochondrial oxidative stress could enhance the ICD to boost cancer immunotherapy[4,20]. During this process, as one of the damage-associated molecular patterns, the exposure of calreticulin (CRT) from the endoplasmic reticulum (ER) to the tumor cell membrane was a symbol of ICD[4,20]. After the treatment with BSA-MHI148@SRF nanoparticles and laser irradiation in MB49 cells, CRT valgus was dramatically increased (Fig. 6F and G), meaning that BSA-MHI148@SRF nanoparticles mediated PDT could amplify the ICD. Because enhanced ICD production and reduced PD-L1 expression both could enhance T cell infiltration and improve its anti-tumor capacity

in vivo, BSA-MHI148@SRF nanoparticles may better reverse the immunosuppression microenvironment *in vivo*.

3.7. Tumor-targeting ability of BSA-MHI148@SRF nanoparticles

To track the pharmacokinetics of BSA-MHI148@SRF nanoparticles *in vivo*, real-time near-infrared fluorescence imaging analysis was performed. As illustrated in Fig. 7A, the fluorescence signal distributed primarily in the whole body at 1 h after the tail vein injection. Then, the fluorescence at the tumor site increased over time, reaching the maximum at 24 h (Fig. 7A). More interestingly, a slightly more MHI148 fluorescence signal at the tumor sites was detected in BSA-MHI148@SRF nanoparticles-administrated mice rather than free MHI148-administrated mice possibly owing to the active tumor targeting capacity of BSA-MHI148, demonstrating the great tumor-targeting effect of the self-assembled BSA-MHI148@SRF nanoparticles (Fig. 7A). Following this, the mice were sacrificed to collect the major organs and tumors for the fluorescence analysis to further assess the bio-distribution of BSA-MHI148@SRF nanoparticles. Results also indicated that both free MHI148 and BSA-MHI148@SRF nanoparticles were mainly distributed in tumor tissues (Fig. 7B and C). Besides, the fluorescence intensity of BSA-MHI148@SRF nanoparticles-treated mice at the tumor site was also a little higher as expected than the free MHI148-administrated mice (Fig. 7B and C). Thus, BSA-MHI148@SRF nanoparticles could selectively accumulate in the tumors *via* active tumor-targeting capability induced by MHI148 and BSA to avoid possible side effects.

3.8. Tumor vessel normalizing ability of BSA-MHI148@SRF nanoparticle

To explore the effect of BSA-MHI148@SRF nanoparticles on tumor vessels, the MB49 tumor model was established to detect the VEGF protein expression in tumor tissues. All the nanoparticles loaded with SRF faded the VEGF fluorescence compared to the vehicle group (Fig. 8A). As we all know, VEGF blockade or inhibition was demonstrated to induce the inhibition of tumor angiogenesis to normalize the remaining abnormal tumor blood vessels[28,29]. Thus, BSA-MHI148@SRF nanoparticles may also induce the tumor vessel normalization as conventional VEGF inhibitors did. As shown in Fig. 8B, after BSA-MHI148@SRF nanoparticles administration, the CD31+ vascular area was attenuated while the vascular maturation sign α-SMA protein was dramatically enhanced, showing that BSA-MHI148@SRF nanoparticles induced the typical tumor vessel normalization characteristic (Fig. 8B). Following this, the protein expression levels in tumors were also further detected by Western blot assay, showing a similar result in line with the fluorescence staining experiments (Fig. 8C and D). All these results indicate that SRF-mediated VEGF inhibition effectively promotes the vascular normalization in tumors, which then could be maximized by tumor-targeting BSA-MHI148@SRF nanoparticles.

D) Expression of Bcl-2 in MB49 tumor cells revealed by Western blot assay and the corresponding protein quantification by ImageJ after treated with PBS, BSA-MHI148, SRF, free MHI148 + laser irradiation, BSA-MHI148 + laser irradiation, BSA-MHI148@SRF, and BSA-MHI148@SRF + irradiation ($n = 3$). (E, F) Relative cell viability of MB49 cells detected by CCK-8 assay after different treatments with or without laser irradiation. Data are demonstrated as mean ± SD. Statistical analysis was performed *via* the two-tail Student's *t*-test. *$P < 0.05$; **$P < 0.01$; ***$P < 0.001$. (+ L) represented the tumor cells treated with 808 nm laser irradiation. (- L) represented the tumor cells treated without 808 nm laser irradiation.
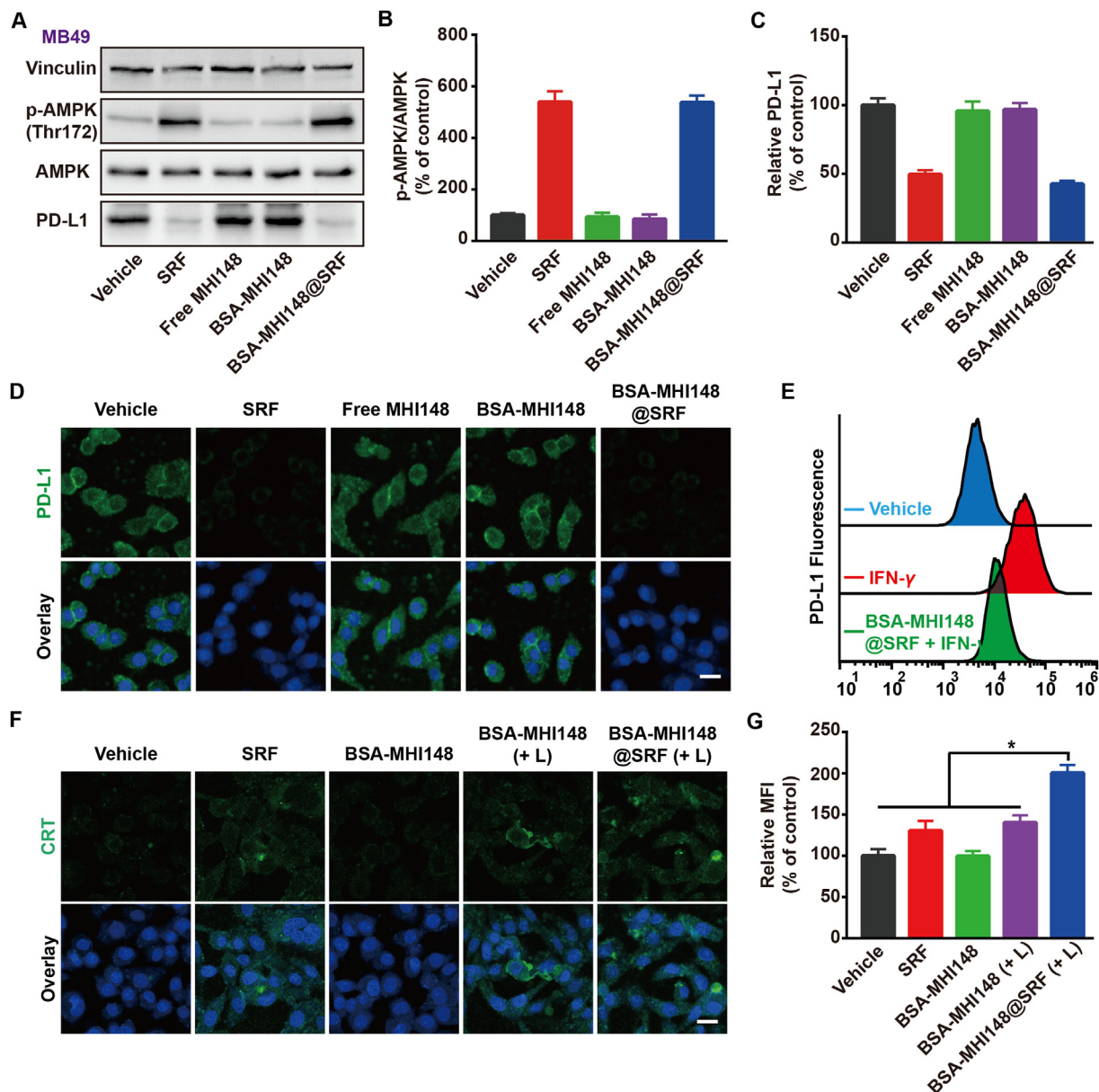
Figure 6   PD-L1 regulation capacity of BSA-MHI148@SRF nanoparticles *in vitro*. (A−C) Expression of the PD-L1 and the p-AMPK protein in MB49 tumor cells revealed by Western blot assay and the corresponding protein quantification by ImageJ after the different treatments for 24 h ($n = 3$). (D) Representative fluorescence images of PD-L1 expression on the MB49 tumor cell membrane after different treatments, scale bar = 20 μm. (E) Cell surface expression of PD-L1 on MB49 tumor cells determined by flow cytometry ($n = 3$). (F) Representative fluorescence images of CRT exposure mediated by various treatments, scale bar = 20 μm. (G) Quantification of various treatments mediated CRT exposure ($n = 3$). Data are demonstrated as mean ± SD. Statistical analysis was performed *via* the two-tail Student's *t*-test. *$P < 0.05$; **$P < 0.01$; ***$P < 0.001$. (+ L) represented the tumor cells treated with laser irradiation.

3.9.   BSA-MHI148@SRF nanoparticle reversed tumor hypoxia microenvironment

Generally, after tumor vessel normalization, the oxygen supply in tumors could be enhanced, leading to the reversed tumor hypoxia microenvironment[28,42]. As we proved just above, BSA-MHI148@SRF nanoparticles could induce tumor vessel normalization. Thus, BSA-MHI148@SRF nanoparticles may reverse tumor hypoxia *via* cascade two-stage tumor re-oxygenation owing to the following mechanisms: (i) SRF encapsulated in BSA-MHI148@SRF nanoparticles decreased tumor oxygen consumption ratio

via inhibiting mitochondria respiratory. (ii) SRF encapsulated in BSA-MHI148@SRF nanoparticles increased the oxygen supply *via* inducing tumor vessel normalization. To confirm our prediction, the expression of tumor hypoxia endogenous indicator hypoxia-inducible factor-1α (HIF-1α) *in vivo* was detected. Surprisingly, after BSA-MHI148@SRF nanoparticles administration *in vivo*, the expression of HIF-1α protein in tumors was most obviously reduced, while BSA or SRF@BSA showed relatively weak effects (Fig. 8E−G). Besides, the inhibition effect of BSA-MHI148@SRF nanoparticles on HIF-1α protein expression without laser irradiation or with irradiation was superior to BSA@SRF nanoparticles
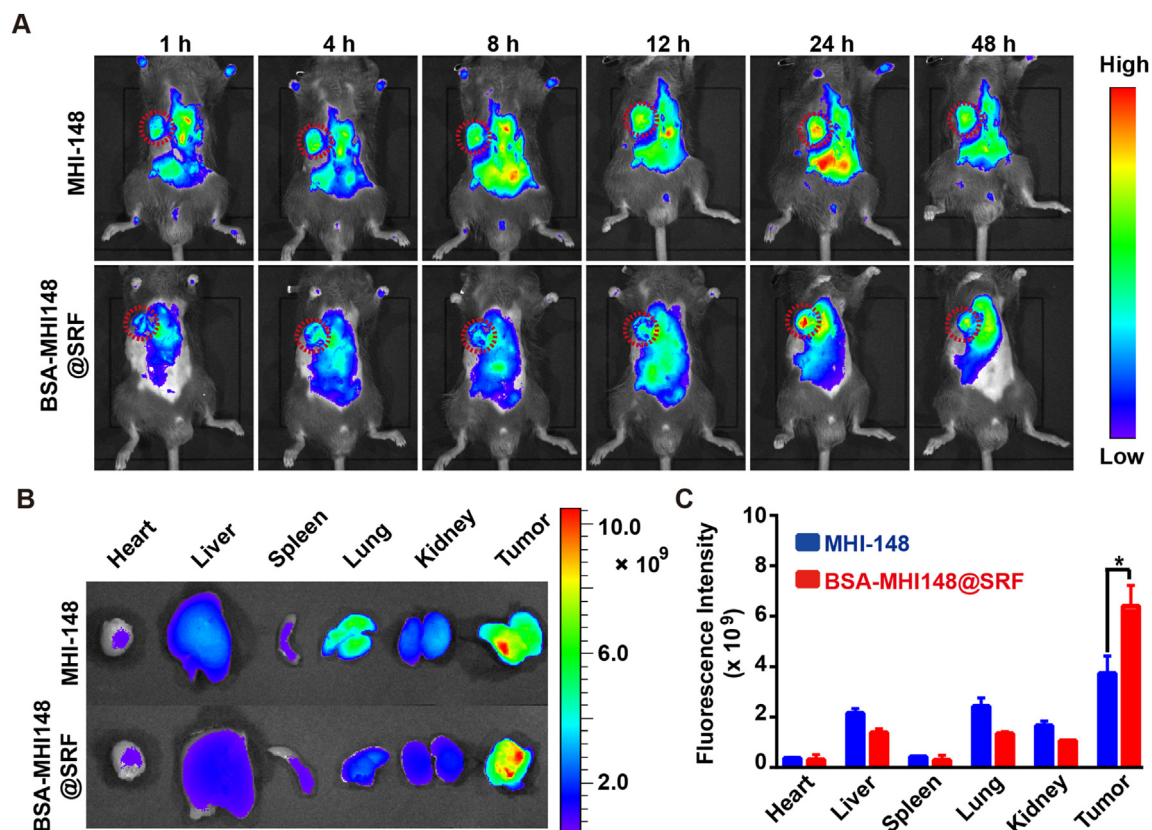
Figure 7 Tumor-targeting ability of BSA-MHI148@SRF nanoparticles. (A) Fluorescence images of MB49 tumor-bearing mice after intravenous injection of BSA-MHI148@SRF nanoparticles and free MHI148 at 1, 4, 8, 12, 24, and 48 h. (B, C) *Ex vivo* fluorescence images of major organs and tumors at 24 h after injection and corresponding quantification of MHI148 fluorescence signal. Data are demonstrated as mean $\pm$ SD. Statistical analysis was performed *via* the two-tail Student's *t*-test. *$P < 0.05$.

given the more ideal tumor-targeted capacity of BSA-MHI148 (Fig. 8E–G, Supporting Information Fig. S20). Moreover, owing to the hypoxia reversion capacity of BSA-MHI148@SRF, the ROS generation of BSA-MHI148@SRF mediated PDT was obviously enhanced compared with the BSA-MHI148 mediated PDT (Supporting Information Fig. S21). Finally, we evaluated the dosage of SRF in the BSA-MHI148@SRF mediated hypoxia reversion. As results indicated, even though the SRF concentration increased to 20 mg/kg (4-fold higher than the dose used in this study), the hypoxia reversion capacity still existed (Supporting Information Fig. S22). Thus, BSA-MHI148@SRF nanoparticles better-reversed tumor hypoxia microenvironment *via* cascade two-stage tumor re-oxygenation induced by SRF encapsulated in it.

3.10. Therapeutic effect of BSA-MHI148@SRF nanoparticles in vitro

To verify the effects of BSA-MHI148@SRF nanoparticles with laser radiation in reversing the immunosuppression tumor microenvironment, we further investigated the surface expression of CRT after BSA-MHI148@SRF nanoparticles with laser irradiation treatment *in vivo*. Results presented that the fluorescence intensity of CRT was much stronger in the BSA-MHI148@SRF nanoparticles with the laser irradiation group, meaning more cell surface CRT exposure was induced by BSA-MHI148@SRF nanoparticles mediated PDT (Fig. 9A). Then, the infiltration of immune cells in tumors was also determined by fluorescence

staining of CD4$^+$ and CD8$^+$ T lymphocytes, showing that the treatment of BSA-MHI148@SRF nanoparticles with laser irradiation dramatically induced the infiltration of T lymphocytes in tumors for the immune killing to tumor cells (Fig. 9A, Supporting Information Fig. S23). Moreover, a similar phenomenon that BSA-MHI148@SRF nanoparticles with laser irradiation most effectively enhanced CD4$^+$ and CD8$^+$ T cell infiltration in MB49 tumors was also revealed by flow cytometry analysis, showing that MHI148@SRF nanoparticles mediated PDT may best enhance photodynamic immunotherapy (Supporting Information Figs. S24 and S25).

However, to our surprise, not what we expected, the PD-L1 expression was not deceased after BSA-MHI148@SRF nanoparticles treatment *in vivo* (Supporting Information Figs. S26 and S27), which was contrary to the conclusion acquired by us *in vitro* (Fig. 3). The reason for this phenomenobecauset that VEFG inhibiting could also up-regulate the expression of PD-L1 by some other mechanisms[43–45]. As previously proved, the increased PD-L1 expression in tumors after conventional VEGF inhibitors was mediated by IFNγ-producing T lymphocytes during VEGF/VEGFR blockade, and the extent of PD-L1 up-regulation correlated with the degree of enhanced T cells activity in the tumors[43,44]. Besides, it was also revealed that the PD-L1 expression was negatively correlated with VEGF in patients with uniformly treated classical Hodgkin lymphoma and breast cancer[43,44,46,47]. In this study, after treatment of BSA-MHI148@SRF nanoparticles, enhanced AMPK phosphorylation mediated PD-L1
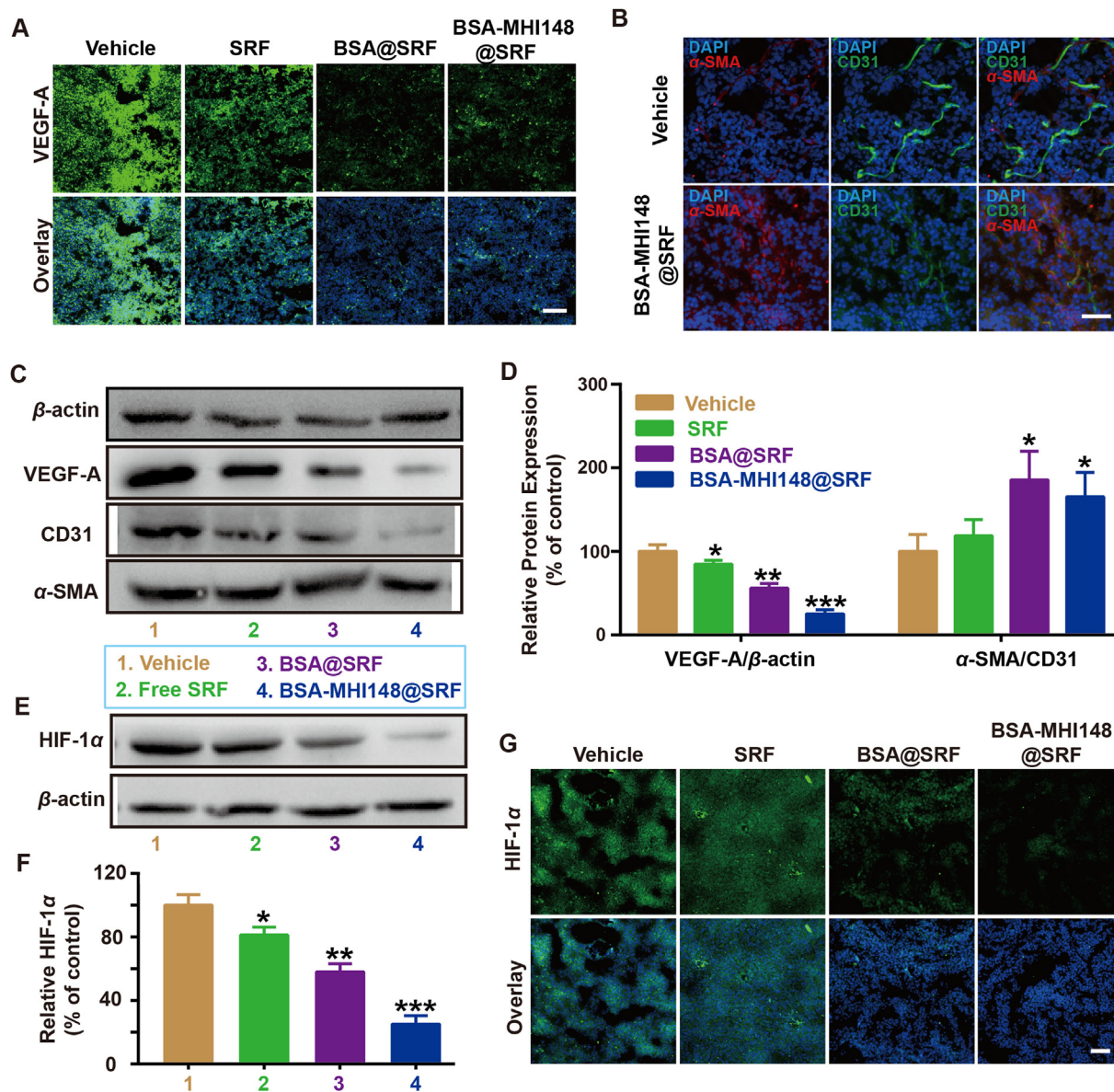
Figure 8 Tumor vessel-normalizing ability and HIF-1α regulation function of BSA-MHI148@SRF nanoparticles *in vivo*. (A) Representative fluorescence images of VEGF-A expression in tumor tissues, scale bar = 100 μm. (B) Representative fluorescence images of α-SMA and CD31 in the tumors treated with MHI148@SRF nanoparticles for 2 days, scale bar = 50 μm. (C, D) Expression of the VEGF-A, α-SMA, and CD31 protein in MB49 tumor tissues revealed by Western blot assay and the corresponding protein quantification by ImageJ after the treatment of BSA@SRF or BSA-MHI148@SRF nanoparticles for 2 days (*n* = 3). (E, F) Expression of the HIF-1α protein in MB49 tumors *in vivo* revealed by Western blot assay and the corresponding protein quantification by ImageJ after the treatment of SRF, BSA@SRF nanoparticles, or BSA-MHI148@SRF nanoparticles for 2 days (*n* = 4). (G) Representative fluorescence images of HIF-1α protein expression in MB49 tumors *in vivo* after the treatment of SRF, BSA@SRF nanoparticles, or BSA-MHI148@SRF nanoparticles for 2 days, scale bar = 100 μm. Data are demonstrated as mean ± SD. Statistical analysis was performed *via* the two-tail Student's *t*-test. *$P < 0.05$; **$P < 0.01$.

down-regulation may be neutralized by the VEGF inhibition amplified PD-L1 upregulation (Figs. S26 and S27). Thus, BSA-MHI148@SRF nanoparticles may inhibit PD-L1 expression *in vitro* rather than *in vivo*, which still needed to be further enhanced by some other VEGF inhibitors.

Interestingly, it was also proved that the depression of VEGF elicited antitumor immunity through enhancing T lymphocytes infiltrating in tumors[46,48–50]. Therefore, the mechanism of enhanced T lymphocytes infiltration of BSA-MHI148@SRF nanoparticles mediated PDT *in vivo* was attributed to the follow-

ing two-stage immune re-sensitization: (i) enhanced immunogenic cell death (ICD) amplified by BSA-MHI148@SRF nanoparticles induced reactive oxygen species (ROS) generation could enhance T cell infiltration and improve its tumor cell killing ability. (ii) BSA-MHI148@SRF nanoparticles induced VEGF inhibition could also obviously reverse tumor immune-suppression microenvironment by causing tumor vessel normalization. Finally, TUNEL staining of tumor tissue sections was also performed to evaluate the tumor cell apoptosis after various treatments. As illustrated in Fig. 9A, BSA-MHI148@SRF nanoparticles with laser radiation resulted in the
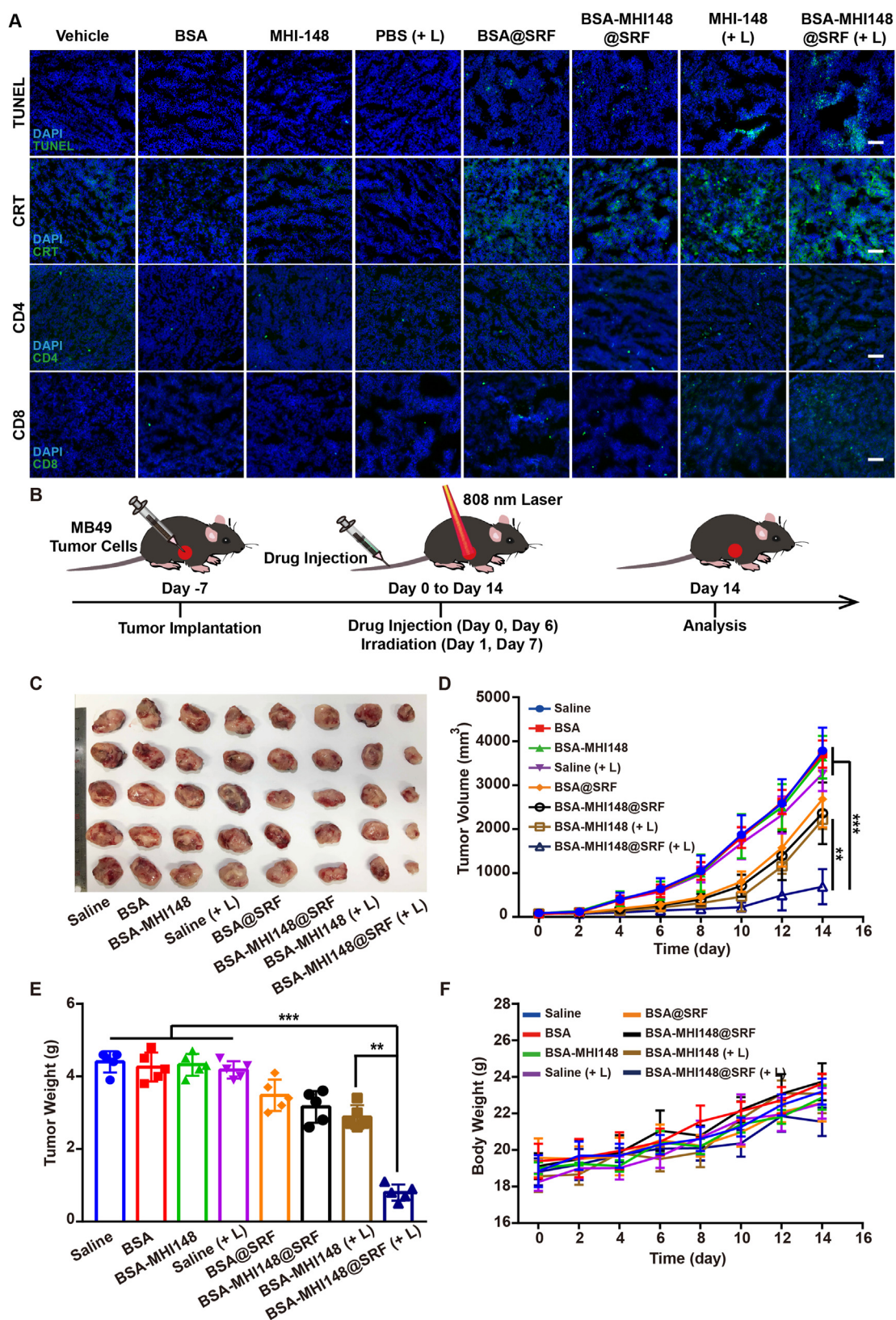
Figure 9 Anti-tumor effect of BSA-MHI148@SRF nanoparticles mediated PDT *in vivo*. (A) Immunofluorescence staining of TUNEL$^+$ tumor cells, CRT, CD4$^+$ T cells, and CD8$^+$ T cells in tumor tissues, scale bars = 100 μm. (B) The schematic diagram of tumor implantation and therapy in mice. (C) Photo of the collected MB49 tumors on Day 14 from all groups ($n = 5$). (D) Volume and (E) Weight of MB49 tumors post-treatment at Day 14 ($n = 5$). (F) Bodyweight changes of mice measured every two days during the treatment period ($n = 5$). Data are demonstrated as mean ± SD. Statistical analysis was performed *via* the two-tail Student's *t*-test. *$P < 0.05$; **$P < 0.01$; ***$P < 0.001$. (+ L) represented the tumors treated with laser irradiation.
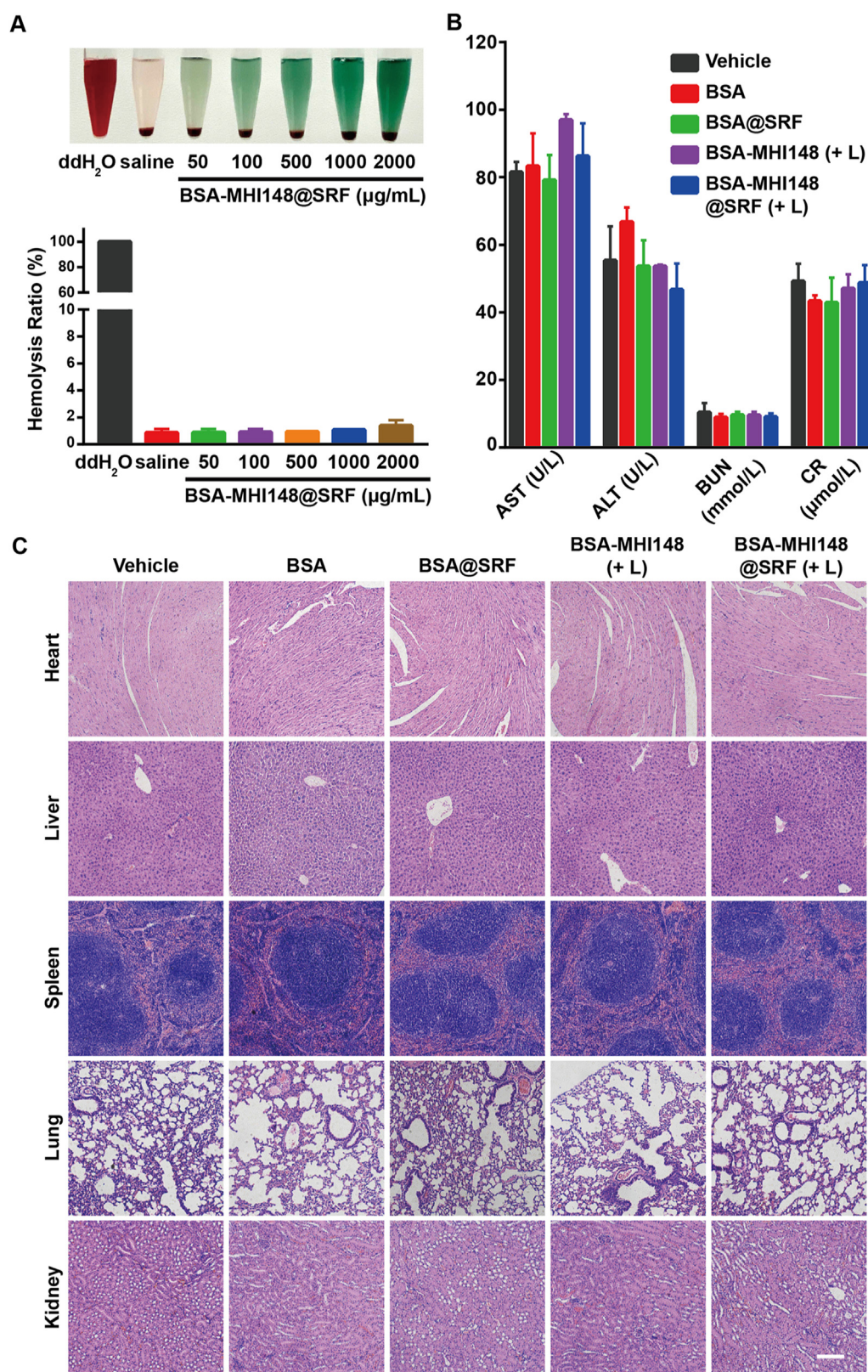
Figure 10 Safety evaluation of BSA-MHI148@SRF nanoparticles *in vivo*. (A) Photographs of hemolysis assay of BSA-MHI148@SRF nanoparticles (double distilled water as the positive control, and saline as the negative control) and corresponding hemolysis rate. (B) Serum biochemistry data of liver function (ALT and AST) and kidney function (BUN and CR) ($n = 3$). (C) Representative H&E images of the major organs (heart, liver, spleen, lung, and kidney) collected from mice after 14 days of various therapies, scale bar $= 100$ μm. Data are demonstrated as mean $\pm$ SD. (+ L) represents the tumors treated with laser irradiation.

most apparent cell apoptosis, followed by BSA-MHI148 with laser radiation and BSA-MHI148@SRF without laser radiation. To sum up, BSA-MHI148@SRF nanoparticles with laser radiation could best induce tumor cell apoptosis *via* the amplified PDT effect and enhanced immune killing effect of T cells.

Inspired by the outstanding tumor-killing effect of BSA-MHI148@SRF nanoparticles *in vitro* and *in vivo*, as well as its perfect tumor-targeting capacity, we then investigated it's *in vivo* anti-tumor growth ability by using MB49 tumor-bearing mice (Fig. 9B). After the 14-day therapy, the tumor growth of mice in the BSA-MHI148@SRF nanoparticles with laser irradiation group was dramatically inhibited in contrast to all other groups (Fig. 9C–E, Supporting Information Fig. S28). Interestingly, BSA-MHI148-@SRF nanoparticles alone without laser irradiation also exerted a slight anti-tumor efficacy, which may be caused by the encapsulated SRF in it (Fig. 9C–E, Fig. S28). In addition, unsatisfied tumor depression effects were presented in the mice treated with BSA-MHI148 and laser irradiation owing to the hypoxia microenvironment in tumor tissues (Fig. 9C–E, Fig. S28). Moreover, in keeping with the results of tumor volume, BSA-MHI148@SRF nanoparticles with laser irradiation also obviously reduced the tumor weight of the mice, while the body weight was not changed obviously compared to other treatments (Fig. 9F). Thus, the fabulous anti-tumor effect in BSA-MHI148@SRF nanoparticles with laser irradiation group indicated that the SRF was able to enhance the PDT efficacy of MHI148 by cascade two-stage tumor re-oxygenation and immune re-sensitization strategy.

3.11. Hemolysis assay and safety evaluation of BSA-MHI148@SRF nanoparticles

At last, the biosafety of BSA-MHI148@SRF nanoparticles was further carefully assessed. Firstly, the hemocompatibility of BSA-MHI148@SRF nanoparticles was determined. As results indicated, BSA-MHI148@SRF nanoparticles possessed fantastic hemocompatibility since no severe hemolysis in red blood cells was induced (Fig. 10A). Subsequently, to evaluate the influence of BSA-MHI148@SRF nanoparticles on the liver and kidney, the index of liver function such as alanine transaminase (ALT) and aspartate transaminase (AST), as well as the index of renal function such as blood urea nitrogen (BUN) and creatinine (CR) were measured (Fig. 10B). As we expected, all function parameters in the BSA-MHI148@SRF nanoparticles with the laser irradiation group were normal and no statistical significance was detected in comparison to the vehicle group (Fig. 10B). Moreover, the hematoxylin and eosin (H&E) staining assay was performed to observe the organization structure of major organs (heart, liver, spleen, lung, and kidney), showing that no significant pathological changes of all organs were caused by BSA-MHI148@SRF nanoparticles (Fig. 10C). Thus, BSA-MHI148@SRF nanoparticles had great clinical application value for tumor therapies with outstanding biosecurity.

4. Conclusions

In this study, we successfully prepared clinical useable cascade two-stage tumor re-oxygenation and immune re-sensitization BSA-MHI148@SRF nanoparticles *via* one-step hydrophilic and hydrophobic self-assembly strategy. The formed BSA-MHI148@SRF nanoparticles with the tumor-targeting photosensitizer MHI148 as ligand presented increased tumor accumulation to refrain from cytotoxicity to normal cells. Benefiting from the SRF encapsulated in the nanoparticles, BSA-MHI148@SRF nanoparticles increased

tumor re-oxygenation *via* two-stage oxygen delivery induced by alleviated tumor oxygen consumption *via* mitochondrial oxidative phosphorylation inhibition and enhanced oxygen perfusion through promoted tumor vessel normalization. In the meanwhile, the mitochondria-targeted MHI148 induced ICD *via* mitochondrial oxidative stress under the irradiation would reverse the tumor immunosuppression microenvironment, which would cooperate with the tumor vessel normalization mediated by SRF to increase the T lymphocytes infiltration and its activity in tumors to sensitize photodynamic immunotherapy. Finally, the tumor-killing efficacy of PDT *in vivo* was strikingly enhanced to eliminate tumors in mice *via* such a well-designed cascade two-stage tumor re-oxygenation and immune re-sensitization strategy. All in all, the multifunctional BSA-MHI148@SRF nanoparticles are supposed to have great potential value for better cancer PDT.

Author contributions

Zaigang Zhou, Jianliang Shen, and Zhiming Li conceived the project. Zaigang Zhou, Jiashe Chen, Yu Liu, Chunjuan Zheng, Wenjuan Luo, Lele Chen, and Shen Zhou performed the experiments and analyzed the results. Jianliang Shen and Zhiming Li provided useful suggestions to this work. Jiashe Chen and Zaigang Zhou wrote the manuscript. Jiashe Chen, Zaigang Zhou, Jianliang Shen, and Zhiming Li discussed the results and reviewed the manuscript.

Conflicts of interest

The authors have no conflicts of interest to declare.

Appendix A. Supporting information

Supporting data to this article can be found online at https://doi.org/10.1016/j.apsb.2022.07.023.

References

1. Liu P, Zhou Y, Shi X, Yuan Y, Peng Y, Hua S, et al. A cyclic nano-reactor achieving enhanced photodynamic tumor therapy by reversing multiple resistances. *J Nanobiotechnol* 2021;**19**:149.
2. Zhang S, Wang Y, Kong Z, Zhang X, Sun B, Yu H, et al. Pure photosensitizer-driven nanoassembly with core-matched PEGylation for imaging-guided photodynamic therapy. *Acta Pharm Sin B* 2021;**11**:3636–47.
3. Li J, Xue Y, Tian J, Liu Z, Zhuang A, Gu P, et al. Fluorinated-functionalized hyaluronic acid nanoparticles for enhanced photodynamic therapy of ocular choroidal melanoma by ameliorating hypoxia. *Carbohydr Polym* 2020;**237**:116119.
4. Wang C, Xiao Y, Zhu W, Chu J, Xu J, Zhao H, et al. Photosensitizer-modified MnO$_2$ nanoparticles to enhance photodynamic treatment of abscesses and boost immune protection for treated mice. *Small* 2020;**16**:e2000589.

5. Fang L, Zhao Z, Wang J, Xiao P, Sun X, Ding Y, et al. Light-controllable charge-reversal nanoparticles with polyinosinic-polycytidylic acid for enhancing immunotherapy of triple negative breast cancer. *Acta Pharm Sin B* 2022;**12**:353−63.

6. Zhang C, Chen W, Zhang T, Jiang X, Hu Y. Hybrid nanoparticle composites applied to photodynamic therapy: strategies and applications. *J Mater Chem B* 2020;**8**:4726−37.

7. Wang X, Wu M, Zhang X, Li F, Zeng Y, Lin X, et al. Hypoxia-responsive nanoreactors based on self-enhanced photodynamic sensitization and triggered ferroptosis for cancer synergistic therapy. *J Nanobiotechnol* 2021;**19**:204.

8. Xiong W, Qi L, Jiang N, Zhao Q, Chen L, Jiang X, et al. Metformin liposome-mediated PD-L1 downregulation for amplifying the photodynamic immunotherapy efficacy. *ACS Appl Mater Interfaces* 2021;**13**:8026−41.

9. Bao R, Wang Y, Lai J, Zhu H, Zhao Y, Li S, et al. Enhancing anti-PD-1/PD-L1 immune checkpoint inhibitory cancer therapy by CD276-targeted photodynamic ablation of tumor cells and tumor vasculature. *Mol Pharm* 2019;**16**:339−48.

10. Wang H, Chao Y, Liu J, Zhu W, Wang G, Xu L, et al. Photosensitizer-crosslinked *in-situ* polymerization on catalase for tumor hypoxia modulation & enhanced photodynamic therapy. *Biomaterials* 2018;**181**:310−7.

11. Gou S, Chen N, Wu X, Zu M, Yi S, Ying B, et al. Multi-responsive nanotheranostics with enhanced tumor penetration and oxygen self-producing capacities for multimodal synergistic cancer therapy. *Acta Pharm Sin B* 2022;**12**:406−23.

12. Zhang X, He C, Sun Y, Liu X, Chen Y, Chen C, et al. A smart O_2-generating nanocarrier optimizes drug transportation comprehensively for chemotherapy improving. *Acta Pharm Sin B* 2021;**11**:3608−21.

13. Zhou Y, Tong F, Gu W, He S, Yang X, Li J, et al. Co-delivery of photosensitizer and diclofenac through sequentially responsive bilirubin nanocarriers for combating hypoxic tumors. *Acta Pharm Sin B* 2022;**12**:1416−31.

14. Li X, Kwon N, Guo T, Liu Z, Yoon J. Innovative strategies for hypoxic-tumor photodynamic therapy. *Angew Chem Int Ed Engl* 2018;**57**:11522−31.

15. Sun Y, Zhao D, Wang G, Wang Y, Cao L, Sun J, et al. Recent progress of hypoxia-modulated multifunctional nanomedicines to enhance photodynamic therapy: opportunities, challenges, and future development. *Acta Pharm Sin B* 2020;**10**:1382−96.

16. Li M, Shao Y, Kim JH, Pu Z, Zhao X, Huang H, et al. Unimolecular photodynamic O_2-economizer to overcome hypoxia resistance in phototherapeutics. *J Am Chem Soc* 2020;**142**:5380−8.

17. Moreno-Sanchez R, Rodriguez-Enriquez S, Marin-Hernandez A, Saavedra E. Energy metabolism in tumor cells. *FEBS J* 2007;**274**:1393−418.

18. Secomb TW, Hsu R, Dewhirst MW. Synergistic effects of hyperoxic gas breathing and reduced oxygen consumption on tumor oxygenation: a theoretical model. *Int J Radiat Oncol Biol Phys* 2004;**59**:572−8.

19. Zhao LP, Zheng RR, Chen HQ, Liu LS, Zhao XY, Liu HH, et al. Self-delivery nanomedicine for O_2-economized photodynamic tumor therapy. *Nano Lett* 2020;**20**:2062−71.

20. Lee D, Kwon S, Jang SY, Park E, Lee Y, Koo H. Overcoming the obstacles of current photodynamic therapy in tumors using nanoparticles. *Bioact Mater* 2022;**8**:20−34.

21. Hu C, He X, Chen Y, Yang X, Qin L, Lei T, et al. Metformin mediated PD-L1 downregulation in combination with photodynamic-immunotherapy for treatment of breast cancer. *Adv Funct Mater* 2021;**31**:2007149.

22. Xia D, Xu P, Luo X, Zhu J, Gu H, Huo D, et al. Overcoming hypoxia by multistage nanoparticle delivery system to inhibit mitochondrial respiration for photodynamic therapy. *Adv Funct Mater* 2019;**29**:1807294.

23. Zhou Z, Jiang N, Chen J, Zheng C, Guo Y, Ye R, et al. Selectively down-regulated PD-L1 by albumin-phenformin nanoparticles mediated mitochondrial dysfunction to stimulate tumor-specific immunological response for enhanced mild-temperature photothermal efficacy. *J Nanobiotechnol* 2021;**19**:375.

24. Shi Q, Li Y, Li S, Jin L, Lai H, Wu Y, et al. LncRNA DILA1 inhibits Cyclin D1 degradation and contributes to tamoxifen resistance in breast cancer. *Nat Commun* 2020;**11**:5513.

25. Phung CD, Tran TH, Pham LM, Nguyen HT, Jeong JH, Yong CS, et al. Current developments in nanotechnology for improved cancer treatment, focusing on tumor hypoxia. *J Control Release* 2020;**324**:413−29.

26. Qin B, Jiang M, Li X, Shi Y, Zhang J, Luo Z, et al. Oxygen nanocarrier broke the hypoxia trap of solid tumors and rescued transfection efficiency for gene therapy. *J Nanobiotechnol* 2021;**19**:427.

27. Fang H, Gai Y, Wang S, Liu Q, Zhang X, Ye M, et al. Biomimetic oxygen delivery nanoparticles for enhancing photodynamic therapy in triple-negative breast cancer. *J Nanobiotechnol* 2021;**19**:81.

28. Ho YJ, Chu SW, Liao EC, Fan CH, Chan HL, Wei KC, et al. Normalization of tumor vasculature by oxygen microbubbles with ultrasound. *Theranostics* 2019;**9**:7370−83.

29. Wu JB, Tang YL, Liang XH. Targeting VEGF pathway to normalize the vasculature: an emerging insight in cancer therapy. *OncoTargets Ther* 2018;**11**:6901−9.

30. Zhang Y, He J. Tumor vasculature-targeting nanomedicines. *Acta Biomater* 2021;**134**:1−12.

31. Jian C, Fu J, Cheng X, Shen LJ, Ji YX, Wang X, et al. Low-dose sorafenib acts as a mitochondrial uncoupler and ameliorates nonalcoholic steatohepatitis. *Cell Metab* 2020;**31**:892−908.

32. Karroum O, Kengen J, Danhier P, Magat J, Mignion L, Bouzin C, et al. Tumor reoxygenation following administration of mitogen-activated protein kinase inhibitors: a rationale for combination with radiation therapy. *Radiother Oncol* 2012;**105**:64−71.

33. Wang Z, Chen L, Ma Y, Li X, Hu A, Wang H, et al. Peptide vaccine-conjugated mesoporous carriers synergize with immunogenic cell death and PD-L1 blockade for amplified immunotherapy of metastatic spinal. *J Nanobiotechnol* 2021;**19**:243.

34. Cha JH, Yang WH, Xia W, Wei Y, Chan LC, Lim SO, et al. Metformin promotes antitumor immunity *via* endoplasmic−reticulum-associated degradation of PD-L1. *Mol Cell* 2018;**71**:606−20.

35. Chen J, Zhou Z, Zheng C, Liu Y, Hao R, Ji X, et al. Chitosan oligosaccharide regulates AMPK and STAT1 pathways synergistically to mediate PD-L1 expression for cancer chemoimmunotherapy. *Carbohydr Polym* 2022;**277**:118869.

36. Ross FA, Hawley SA, Auciello FR, Gowans GJ, Atrih A, Lamont DJ, et al. Mechanisms of paradoxical activation of AMPK by the kinase inhibitors SU6656 and Sorafenib. *Cell Chem Biol* 2017;**24**:813−824 e4.

37. Chen F, Fang Y, Chen X, Deng R, Zhang Y, Shao J. Recent advances of sorafenib nanoformulations for cancer therapy: smart nanosystem and combination therapy. *Asian J Pharm Sci* 2021;**16**:318−36.

38. Li Q, Shi Z, Zhang F, Zeng W, Zhu D, Mei L. Symphony of nanomaterials and immunotherapy based on the cancer-immunity cycle. *Acta Pharm Sin B* 2022;**12**:107−34.

39. Zhang C, Liu T, Luo P, Gao L, Liao X, Ma L, et al. Near-infrared oxidative phosphorylation inhibitor integrates acute myeloid leukemia-targeted imaging and therapy. *Sci Adv* 2021;**7**:eabb6104.

40. Wu JB, Shao C, Li X, Shi C, Li Q, Hu P, et al. Near-infrared fluorescence imaging of cancer mediated by tumor hypoxia and HIF1alpha/OATPs signaling axis. *Biomaterials* 2014;**35**:8175−85.

41. Huang QJ, Liao GC, Zhuang XR, Yang ML, Yao JJ, Deng JH, et al. Ras inhibitor farnesylthiosalicylic acid conjugated with IR783 dye exhibits improved tumor-targeting and altered anti-breast cancer mechanisms in mice. *Acta Pharmacol Sin* 2022;**43**:1843−56.

42. Chang CC, Dinh TK, Lee YA, Wang FN, Sung YC, Yu PL, et al. Nanoparticle delivery of MnO_2 and antiangiogenic therapy to overcome hypoxia-driven tumor escape and suppress hepatocellular carcinoma. *ACS Appl Mater Interfaces* 2020;**12**:44407−19.

43. Schmittnaegel M, Rigamonti N, Kadioglu E, Cassara A, Wyser Rmili C, Kiialainen A, et al. Dual angiopoietin-2 and VEGFA inhibition elicits antitumor immunity that is enhanced by PD-1 checkpoint blockade. *Sci Transl Med* 2017;**9**:eaak9670.

44. Allen E, Jabouille A, Rivera LB, Lodewijckx I, Missiaen R, Steri V, et al. Combined antiangiogenic and anti-PD-L1 therapy stimulates tumor immunity through HEV formation. *Sci Transl Med* 2017;**9**:eaak9679.

45. Ren D, Hua Y, Yu B, Ye X, He Z, Li C, et al. Predictive biomarkers and mechanisms underlying resistance to PD1/PD-L1 blockade cancer immunotherapy. *Mol Cancer* 2020;**19**:1−19.

46. Fankhauser M, Broggi MAS, Potin L, Bordry N, Jeanbart L, Lund AW, et al. Tumor lymphangiogenesis promotes T cell infiltration and potentiates immunotherapy in melanoma. *Sci Transl Med* 2017;**9**: eaal4712.

47. Liu Y, Liu X, Zhang N, Yin M, Dong J, Zeng Q, et al. Berberine diminishes cancer cell PD-L1 expression and facilitates antitumor immunity *via* inhibiting the deubiquitination activity of CSN5. *Acta Pharm Sin B* 2020;**10**:2299−312.

48. Yang J, Yan J, Liu B. Targeting VEGF/VEGFR to modulate antitumor immunity. *Front Immunol* 2018;**9**:978.

49. Meder L, Schuldt P, Thelen M, Schmitt A, Dietlein F, Klein S, et al. Combined VEGF and PD-L1 blockade displays synergistic treatment effects in an autochthonous mouse model of small cell lung cancer. *Cancer Res* 2018;**78**:4270−81.

50. Bao X, Shen N, Lou Y, Yu H, Wang Y, Liu L, et al. Enhanced anti-PD-1 therapy in hepatocellular carcinoma by tumor vascular disruption and normalization dependent on combretastatin A4 nanoparticles and DC101. *Theranostics* 2021;**11**:5955−69.